Large Fe isotope fractionations in sulfide ores and ferruginous sedimentary rocks from the Kuroko volcanogenic massive sulfide deposits in the Hokuroku district, northeast Japan

Tsubasa Otake[1*], Ryoichi Yamada[2], Ryohei Suzuki[1], Shunsuke Nakamura[1], Akane Ito[3], Ki-cheol Shin[4], Tsutomu Sato[1]

[1]Division of Sustainable Resource Engineering, Faculty of Engineering, Hokkaido University, N13W8, Kita-ku, Sapporo, Hokkaido, 060-8628, Japan

[2]Graduate School of Environmental Studies, Tohoku University, Aramaki 6-6, Aoba-ku, Sendai, Japan, 980-8579

[3]Department of Applied Chemistry for Environment, School of Science and Technology, Kwansei Gakuin University, Gakuen 2-1, Sanda, Hyogo, 669-1337, Japan

[4]RIHN Center, Research Institute for Humanity and Nature, 457-4 Motoyama, Kamigamo, Kita-ku, Kyoto, 603-8047, Japan

*Corresponding author: Tsubasa Otake

Division of Sustainable Resources Engineering, Faculty of Engineering, Hokkaido University, N13W8, Kita-ku, Sapporo, Hokkaido, 060-8628, Japan

Phone: 011-706-6323; fax: 011-706-6323; e-mail: totake@eng.hokudai.ac.jp

Abstract

Anoxic seawater may have played an important role in the preservation of volcanogenic massive sulfide (VMS) deposits in the Hokuroku district, northeast Japan, which is the type locality for Kuroko-type VMS deposits. In this study, we investigated the Fe isotopic compositions of sulfide ores and overlying ferruginous sedimentary rocks in these deposits. These data, coupled with petrographic and geochemical data, enable us to investigate the key formation processes and conditions during the formation of large Kuroko-type VMS deposits. Large Fe isotope variations of ca. 4‰ (δ^{56}Fe) associated with negative or positive Ce anomalies characterize the ferruginous sedimentary rocks formed in the Kuroko VMS deposits and post-Kuroko hydrothermal activity. This suggests that iron (hydr)oxides were precipitated by the partial oxidation of dissolved Fe^{2+} derived from hydrothermal fluids in anoxic or suboxic pools in the Hokuroku Basin. Positive Eu anomalies in the ferruginous cherts closely associated with the Kuroko VMS deposits indicate formation from high-temperature hydrothermal fluids. Zinc-rich black ores in both the Matsumine and Fukazawa deposits have lower δ^{56}Fe values, due to rapid precipitation of pyrite triggered by the mixing of hydrothermal fluids with seawater. Positive shifts in δ^{56}Fe values in the ferruginous cherts from the Ezuri and Fukazawa deposits may be explained by simultaneous precipitation of ferruginous sedimentary rocks with black ores, which modified the δ^{56}Fe values of the hydrothermal fluids to positive values. However, Cu-rich yellow ores show no significant Fe isotope fractionation as compared with the dissolved Fe in the hydrothermal fluids, and were likely formed by slow growth of pyrite that replaced the black ores. The difference in the abundance of sulfide ores between the Matsumine and Fukazawa deposits may reflect the duration of hydrothermal circulation.

Keywords: Volcanogenic massive sulfide deposit; Redox environment; Seafloor hydrothermal system; Fe isotopes; Rare earth elements

Highlights

- Fe isotopes were variable in ferruginous rocks during and after Kuroko formation
- Anoxic pools in Hokuroku Basin may have facilitated preservation of sulfide ores
- Prominent Eu anomalies in ferruginous rocks indicate association with VMS deposits
- Fe isotopes in Zn-rich black ores are negatively shifted due to a kinetic effect
- Duration of hydrothermal circulation is a primary control on ore grade and tonnage

1. Introduction

Volcanogenic massive sulfide (VMS) or volcanic-hosted massive sulfide (VHMS) deposits are important sources of base metals (e.g., Cu, Zn, and Pb) and precious metals (e.g., Ag and Au) worldwide. In general, VMS deposits have been considered to be stratabound hydrothermal deposits (i.e., associated with submarine volcanism and hydrothermal activity that was contemporaneous with deposition of the host volcanic and/or sedimentary rocks) and thus primarily formed on or near the seafloor by mixing of venting hydrothermal fluids with seawater (e.g., Franklin et al., 1981; Franklin et al., 2005; Shanks and Thurston, 2012). VMS deposits are subdivided, based on tectonic setting and/or host-rock composition, into bimodal–mafic, bimodal–silicic, siliciclastic–silicic, and pelitic–mafic types (e.g., Franklin et al., 2005; Shanks and Thurston, 2012). Numerous previous studies have been conducted on VMS deposits, which focused on their geodynamic setting, geology, volcanology, geochemistry (e.g., H, O, S, Sr, and Pb

isotopes), geochronology, ore mineralogy and paragenesis, hydrothermal fluids, and host rock alteration, in order to construct models for ore formation and facilitate exploration (Franklin et al., 1981; Ohmoto and Skinner, 1983; Ohmoto, 1996; Large et al., 2001; Franklin et al., 2005; Shanks and Thurston, 2012; Tornos et al., 2015 and referenes therein).

One focus of the study is the redox condition of ancient seawater during the formation of VMS deposits. Given that most VMS deposits are thought to form on the seafloor, long-term exposure to oxygenated seawater during ore body formation or before burial by overlying sediments would oxidize and dissolve the sulfide ore bodies. Therefore, some previous studies have proposed that anoxic or suboxic water conditions, which occurred either globally during the Precambrian or oceanic anoxic events (e.g., Slack et al., 2007; Slack et al., 2009; Nozaki et al., 2013), or locally (e.g., Goodfellow et al., 2003; Komuro et al., 2004; Menor-Salván et al., 2010), had an important role in the preservation of sulfide ores in VMS deposits. Various geochemical proxies have been used to infer the redox state of marine environments, such as S isotopes and redox-sensitive elements in the overlying clastic sedimentary rocks (e.g., mudstones; Goodfellow et al., 2003). However, the geochemical signatures of the overlying chemical sedimentary rocks (i.e., exhalates; Slack, 2012) may provide more robust information on the geochemical conditions of hydrothermal fluids and seawater. These sediments are the products of fluid mixing and contain iron (hydr)oxides, including goethite and hematite, which sequester trace elements, such as rare earth elements (REEs; Miller et al., 2001; Grenne and Slack, 2005; Slack et al., 2007; Slack et al., 2009).

The Hokuroku district, located in the northeastern Honshu arc in Japan, is a region where a cluster of VMS deposits have been found and were mined until the 1990s.

These deposits were formed in the late stages of back-arc rifting of the northeastern Honshu arc system in the middle Miocene. This is the type locality for Kuroko-type VMS deposits (Cox and Singer, 1986). This type is equivalent to the bimodal–silicic type deposit (e.g., Franklin et al., 2005). A typical Kuroko VMS deposit exhibits distinct ore zoning from top to bottom: barite, black, yellow, pyrite, and siliceous ores. The economically important ores are the black ore (sphalerite–galena–chalcopyrite–pyrite–barite) that is enriched in Zn and Pb and yellow ore (pyrite–chalcopyrite) that is enriched in Cu (Sato, 1974). The outermost zone is typically overlain by thin ferruginous cherts, which are called “tetsusekiei” (translated literally from Japanese this means iron quartz) that are interpreted as being exhalates (Kalogeropoulos and Scott, 1983). Only a few Kuroko VMS deposits (e.g., Matsumine and Doyashiki) in the Hokuroku district contain all the ore zones (Franklin et al., 1981). The other deposits (e.g., Ainai, Fukazawa, and Ezuri) do not contain large pyrite or yellow ore zones. This distinct ore zonation has been explained by a replacement growth model (Eldridge et al., 1983; Ohmoto, 1996), in which Cu-bearing high-temperature (>300°C) hydrothermal fluid replaces the interior of pre-existing black ore during the growth of ore bodies. This model has been generally accepted, although Urabe and Marumo (1991) suggested that yellow ore formation preceded black ore formation based on Pb isotope systematics of the ores.

The Hokuroku district contains a depression structure (i.e., the Hokuroku Basin) that formed from submarine calderas (Ohmoto and Takahashi, 1983). Caldera formation may have had a key role in the generation of large fracture systems for hydrothermal circulation and, possibly, local anoxic pools for the preservation of sulfide ore bodies. Komuro et al. (2004) suggested that anoxic pools only occurred locally in the vicinity of Kuroko VMS deposits in the ore horizon in the Hokuroku Basin, based on S isotopes and

117 trace fossils in overlying mudstones. However, there is no other evidence for the former
118 presence of anoxic water in the Hokuroku district. Ferruginous and/or ferromanganese
119 sedimentary rocks have been recognized in the younger sedimentary rocks, which formed
120 due to post-Kuroko hydrothermal activity (Tsukamoto et al., 2020). Consequently, a
121 comparison of the geochemical characteristics of such rocks associated with the Kuroko
122 VMS deposits might provide insights into the sedimentary environments in the Hokuroku
123 Basin. Moreover, such a comparison might reveal the key factors involved in the
124 formation and preservation of VMS deposits.

125 Stable Fe isotopes have been recently widely used to understand geochemical
126 conditions and processes involving Fe during both biological and non-biological
127 processes under various conditions (Dauphas et al., 2017 and references therein). In
128 geological samples, chemical sediments show the largest Fe isotope variations (Beard and
129 Johnson, 2004), due to the effects of redox reactions (dissolved Fe^{2+} to Fe^{3+} hydroxides)
130 in an open system (i.e., the ocean), such as Precambrian banded iron formations (BIFs).
131 Iron isotope variations in BIFs have been interpreted to reflect partial oxidation in a
132 redox-stratified ocean (e.g., Planavsky et al., 2009), bacterial iron reduction (e.g.,
133 Heimann et al., 2010), or sequestration of isotopically light Fe by sulfide precipitation
134 (e.g., Rouxel et al., 2005). Ferruginous cherts associated with VMS deposits may have
135 formed by similar geochemical processes (Slack et al., 2007), meaning that Fe isotope
136 data for the cherts might provide insights into the conditions of the mineralizing
137 hydrothermal fluids and seawater. Furthermore, Fe isotopic compositions of sulfide ores
138 might also reveal the formation processes of the VMS ore bodies and overlying
139 ferruginous cherts. Recent Fe isotope studies have been conducted on numerous sulfide
140 ore deposits, including orthomagmatic Ni deposits (e.g., Hofmann et al., 2014), magmatic

141 to hydrothermal Fe deposits (e.g., Günther et al., 2017), porphyry Cu and Sn–W deposits
142 (e.g., Wawryk and Foden, 2015; Li et al., 2018a; He et al., 2020), skarn deposits (e.g.,
143 Zhu et al., 2016), and hydrothermal Pb–Zn and Au deposits (Wang et al., 2017; Zhu et al.,
144 2018). However, few Fe isotope studies have been conducted on VMS, sedimentary
145 exhalative (SEDEX), or Mississippi Valley-type (MVT) deposits (Gagnevin et al., 2012),
146 all of which were formed by submarine hydrothermal activity. In contrast, sulfide deposits
147 on the modern seafloor have been investigated (e.g., Rouxel et al., 2004; Rouxel et al.,
148 2008; Li et al., 2018b).

149 The objectives of this study were to understand the redox state of seawater in the
150 Hokuroku Basin, and investigate whether it had an important role in the preservation of
151 sulfide ore bodies, based on Fe isotope compositions of the overlying ferruginous cherts
152 and younger sedimentary rocks, along with petrographic and geochemical data. Specific
153 trends in Fe isotopes and other geochemical data (e.g., REE patterns) associated with
154 VMS deposits can be used as a guide for ore deposit exploration. We also determined the
155 Fe isotope compositions of various sulfide ores (black and yellow ores) in the Kuroko
156 VMS deposits to investigate the relationships between the sulfide ore bodies and
157 ferruginous cherts. A comparison between Kuroko VMS deposits with different styles of
158 mineralization (e.g., tonnage and dominant ore zone) may also provide insights into the
159 key factors responsible for the formation of large Kuroko VMS deposits.

160

161 **2. Geological background**

162 The detailed geology of the Hokuroku district was described by Tanimura et al.
163 (1983) and, more recently, by Yamada and Yoshida (2004; 2011). The basement consists
164 of a Jurassic accretionary complex and Paleogene granitic rocks, which are

unconformably overlain by andesitic lava flows and tuffs (Fig.1; after Yamada et al., 2012). Extensive bimodal volcanism associated with back-arc tectonism is evident as alternating basaltic lava flows (B2 and B3) and felsic (dacite–rhyolite) tuffs (T1–T4), and felsic intrusions (R1–R4). Mudstones (M1–M3) were deposited between the volcanic units and alternate with the felsic tuffs. In particular, the M2 mudstone is distributed throughout the Hokuroku Basin.

Kuroko VMS deposits were formed in a specific horizon in the Hokuroku district, and are mostly hosted in the T3 tuff and overlain by the M2 mudstone. The deposits were generally associated with extensive hydrothermal activity related to R3 rhyolite domes (Fig. 1). The M2a mudstone is intercalated with felsic (R2) and basaltic lava flows (B2), which overlie some of the VMS deposits, such as the Fukazawa deposit (Yamada and Yoshida, 2011). Although VMS mineralization (e.g., Matsumine, Doyashiki, and Kosaka) occurs mostly in the western and eastern parts of the Hokuroku Basin, a few deposits (e.g., the Fukazawa and Ezuri deposits) also occur in the central part of the basin.

The younger sedimentary rocks comprise alternating beds of pumice tuff (T2) and mudstone (M1b), as well as fine-grained tuff (T1) and siltstone (M1a; Fig. 1), which were intruded by felsic magmas (R1). Although no VMS deposits have been discovered in the younger sedimentary rocks, hydrothermal activity (i.e., post-Kuroko hydrothermal activity) is evident as Mn mineralization (Tsukamoto et al., 2020), as well as ferruginization and silicification of the sedimentary rocks.

3. Samples and methodology

3.1. Samples

Ferruginous sedimentary rocks were obtained from three different stratigraphic

189 units in the Hokuroku district. They are classified into three groups based on the
190 stratigraphy and their association with sulfide mineralization.

191 Group A samples are ferruginous cherts associated with the Kuroko VMS
192 deposits. Group A samples were mostly obtained from closed underground mines of the
193 Doyashiki (DY), Kosaka (KS), Matsumine (MT), Ezuri (EZ), and Fukazawa (FZ)
194 deposits, which were provided by the DOWA Metal & Mining (DOWA) and Tohoku
195 University. However, samples from the Kannondo deposit were obtained from an outcrop
196 as this deposit has not been mined and is accessible on the surface. The samples from the
197 Kannondo and Doyashiki deposits (Kitazono and Ueno, 2003) were combined (DY1 to
198 DY10; Supplementary Table 1), as these deposits are located close to each other.

199 Group B samples are ferruginous and/or ferromanganese sedimentary rocks
200 formed during post-Kuroko hydrothermal activity in the T2 or M2 unit, which are from
201 Nittobe (NT), Nagatoro (NR), and Koyukisawa (KY). Although some samples contain
202 significant amounts of detrital and tuffaceous components (e.g., NR3 and KY5), the other
203 samples are cherty and appear to be typical ferruginous cherts closely associated with
204 VMS deposits (e.g., NT3 and KY10). All the samples were obtained from outcrops,
205 except for KY8, which was obtained from a drill core.

206 Group C samples are ferruginous sedimentary rocks in the younger M1 mudstone,
207 from Shinekari (SN) and Daimyojin (DM). Both samples are reddish silicified siltstones
208 that were collected from outcrops.

209 Sulfide ore samples from the contrasting Matsumine and Fukazawa deposits were
210 examined, both of which were also obtained from DOWA and Tohoku University. All the
211 sulfide ore samples were originally taken from underground mines operated by DOWA.
212 The Matsumine deposit was estimated to have ca. 24 million tons (Mt) of ore reserves

(reserves + possible reserves) in 1971, including ca. 10 Mt of yellow ore (2.4 wt.% Cu) and 2.3 Mt of black ore (9.4 and 3.8 wt.% of Zn and Pb, respectively). The Fukazawa deposit was estimated to have 2.4 Mt of ore reserves in 1984, including 0.3 Mt of yellow ore (1.5 wt.% Cu) and 1.0 Mt of black ore (22.4 and 5.5 wt.% of Zn and Pb, respectively). Therefore, the Matsumine deposit can be described as a yellow ore-rich (i.e., Cu-rich), large-sized deposit, whereas the Fukazawa deposit is a black ore-rich, medium-sized deposit (Ohmoto, 1996; Mosier et al., 2009). Representative black ores (sphalerite- and galena-rich) and yellow ores (chalcopyrite-rich) were obtained from each deposit. Pyrite-rich ores from the Matsumine deposit were also analyzed.

3.2. Analytical methods

Polished thin-sections and thick-sections were examined with an Olympus BX60 optical microscope. Mineral identification was verified with a scanning electron microscope (SUPERSCAN SSX-550, Shimadzu). Whole-rock major element compositions of the ferruginous sedimentary rocks were determined by X-ray fluorescence (XRF; MagiX PRO; PANalytical) spectrometry with a Rh tube. The powdered samples were heated for 20 h at 1050°C to remove volatile components and calculate loss-on-ignition (LOI) values. A mixture of 0.4 g of dried sample and 4 g of $Li_2B_4O_7$ was then placed in a Pt crucible, heated at 1000°C for 8 min in a TK-4100 bead sampler, and then cooled, resulting in a fused glass disc that was used for whole-rock XRF analysis.

Trace element concentrations of the ferruginous sedimentary rocks and major and trace element concentrations of the sulfide ores were determined by inductively coupled plasma atomic emission spectroscopy (ICP-AES; ICPE-9000; Shimadzu) and

ICP mass spectrometry (ICP-MS; iCap Qc; Thermo Scientific) on acid-digested samples using the method of Yokoyama et al. (1999). Rhodium was used as an internal standard for the ICP-MS analysis. Although we attempted to achieve total digestion of the solid samples, some samples had residues, which were likely insoluble barite. Given that Ba oxides ($^{135}Ba^{16}O^{+}$) are known to interfere with Eu ($^{151}Eu^{+}$) during ICP-MS analysis, we did not attempt further processing to achieve complete dissolution. Oxide formation was monitored with the CeO/Ce ratio and maintained below 0.5% to minimize oxide interferences. Samples containing 1000–5000 ppm Ba were corrected for the isobaric interference on ^{151}Eu. For samples with >5000 ppm Ba, Eu concentrations are considered unreliable, and therefore their REE patterns are not reported. Manganese concentrations are only reported for the ferruginous sedimentary samples that were below the detection limits of the XRF analysis, as XRF data are more reliable at higher Mn concentrations. Ce and Eu anomalies (Ce/Ce* and Eu/Eu*) in REE patterns normalized to Post-Archean Australian Shale (PAAS; McLennan, 1989) were calculated based on these equations:

$$Ce/Ce^* = Ce_{(SN)}/(0.5La_{(SN)} + 0.5Pr_{(SN)}) \quad (1) \text{ and}$$

$$Eu/Eu^* = Eu_{(SN)}/(0.66Sm_{(SN)} + 0.33Tb_{(SN)}) \quad (2),$$

where $La_{(SN)}$, $Ce_{(SN)}$, $Pr_{(SN)}$, $Sm_{(SN)}$, $Eu_{(SN)}$, and $Tb_{(SN)}$ are PAAS-normalized values for each element (Planavsky et al., 2010).

Iron isotopic compositions were measured with a multi-collector (MC)-ICP-MS (Neptune Plus, Thermo Scientific) at the Research Institute for Humanity and Nature (RIHN), Kyoto, Japan. Iron was purified from acid-digested samples by chromatographic separation using columns compacted with anion exchange resin (AG1-X8 200–400 mesh; Bio-Rad) followed the method of Ito et al. (2017), which in turn was modified after Borrok et al. (2007). Dissolved samples were loaded onto the columns with 1 mL of 8 M

HCl, and the matrix was eluted with 5 mL of 8 M HCl and 5 mL of 3 M HCl. Iron was collected in 4 mL of 0.4 M HCl. The purification process was performed twice for the ferruginous sedimentary rock samples and three times for the sulfide ore samples. Finally, the samples were re-dissolved and diluted in 1% HNO_3 to obtain 10 mL of 0.5 ppm Fe solutions.

Iron isotope ratios were obtained in medium-resolution mode (M/ΔM = 8000–9000) to avoid the major isobaric interferences of $^{40}Ar^{14}N^+$, $^{40}Ar^{16}O^+$, and $^{40}Ar^{16}OH^+$ on ^{54}Fe, ^{56}Fe, and ^{57}Fe, respectively (Weyer and Schwieters, 2003). Interferences of $^{54}Cr^+$ on $^{54}Fe^+$ and $^{58}Ni^+$ on $^{58}Fe^+$ were corrected using $^{54}Cr/^{52}Cr = 0.0282$ and $^{58}Ni/^{60}Ni = 2.616$ (Beard and Johnson, 1999). The isotope ratios are reported using the delta notation as the per mil (‰) deviation of the $^{56}Fe/^{54}Fe$ ratio of the samples relative to that of IRMM-014b (Institute for Reference Materials and Measurements) using the following equation:

$$\delta^{56}Fe_{IRMM\text{-}014b} = [(^{56}Fe/^{54}Fe)_{sample}/(^{56}Fe/^{54}Fe)_{IRMM\text{-}014b} - 1] \times 10^3 \quad (3)$$

The reproducibility of the samples was better than ±0.10‰ (2σ). External reproducibility of our laboratory reference material (Merck Fe solution) was ±0.11‰ (2σ, n = 36).

4. Results

4.1. Petrography and mineralogical compositions

The ferruginous sedimentary rocks are typically composed of microcrystalline hematite and quartz, although acicular iron oxide crystals, which are possibly pseudomorphs of goethite, were also found in some samples (Fig. 2a). These ferruginous cherts are typical of Group A samples, which are associated with Kuroko VMS deposits (e.g., DY2, EZ1, EZ4, and FZ2), but also characterize some Group B and C samples (e.g., NT2 and SN1). The ferruginous cherts also contain minor amounts of pyrite (±other

sulfide minerals, such as sphalerite and chalcopyrite). Some Group A samples (e.g., DY1, KS3, and MT1; Fig. 2b) contain significant amounts of barite in addition to the sulfide minerals. Other Group A samples (KS2, DY7, and MT2; Fig. 2c) contain unaltered and altered detrital minerals (e.g., plagioclase, sericite, quartz, and ilmenite) and tuff fragments (e.g., zeolite and chlorite). Barite is more prominent in samples that are more closely associated with the sulfide ore bodies. Detrital minerals were common in Group B and C samples, and also those Group A samples distal from the ore bodies. However, hematite occurs interstitial to microcrystalline quartz in these samples. Group B samples from Koyukisawa (KY) are tuffaceous, but also contain microcrystalline hematite as well as Mn-bearing calcite (e.g., KY8). Some samples also contain significant amounts of Mn-bearing minerals (e.g., DY10, EZ5, and MT3; Fig. 2d). The blackish areas of these samples are mostly dominated by Mn oxides, and Mn is also hosted by carbonate and silicate minerals. Manganese-bearing carbonate minerals may have colloform structures, with alternating layers of hematite (or goethite) and microcrystalline quartz (Fig. 2d).

Black ores are composed predominantly of sphalerite, pyrite, and galena, which are finely intergrown though larger sphalerite grains that contain minute pyrite crystals (Fig. 2e). Pyrite is either euhedral or anhedral, and occasionally has a colloform texture. Some sphalerite and galena also have a dendritic texture. Barite forms large euhedral crystals and occupies the interstices of sulfide minerals. Copper-bearing minerals are dominated by chalcopyrite, whereas some samples also contain tetrahedrite. No significant difference in the petrography of the black ores was observed between the Fukazawa and Matsumine deposits, except for one sample from Matsumine (MT57) containing abundant bornite and chalcocite. Yellow ores are predominantly composed of large euhedral crystals of pyrite and interstitial chalcopyrite (Fig. 2f). Although yellow

ores are rare in the Fukazawa deposit, the mineralogical compositions and textures are similar in the Fukazawa and Matsumine deposits. The petrography of the pyrite ores is similar to that of the yellow ores, but contain significantly less chalcopyrite and are mostly dominated by large euhedral pyrite crystals.

4.2. Major and trace elements

The ferruginous sedimentary rocks have variable Fe_2O_3 contents from <1 wt.% to 56 wt.% (Supplementary Table 1). The Group A samples have a wider range of Fe_2O_3 contents than the other groups (Fig. 3a). Group C samples tend to have lower Fe_2O_3 contents. Al_2O_3 contents are also variable, ranging from below XRF detection limits (<0.05 wt.%) to 17 wt.%, similar to values for normal clastic sedimentary rocks (e.g., 18.9 wt% for PAAS; Condie, 1993). Group A samples have a lower median value for Al_2O_3 contents than Group B and C samples (Fig. 3b). MnO is the most variable component, with a concentration range of five orders of magnitude (Fig. 3c). Although a few Mn-rich samples in Group A contain up to 50 wt.% MnO, Group B samples tend to have higher MnO contents than Group A samples on average.

Some Group A samples are rich in transition metals, such as Cu and Zn, with values exceeding 1 wt.% (10,000 ppm; e.g., DY1, KS3, and MT1; Supplementary Table 2-1). Barium concentrations are also high (>1 wt.%) in some samples, although some barite-rich samples do not have high Ba concentrations (e.g., KS4 and MT1), indicating incomplete dissolution of barite during sample digestion. Total REE (ΣREE) concentrations vary from 0.5 to ca. 200 ppm (Supplementary Tables 2-1 and 2-2), as compared with the ΣREE concentration of PAAS of 185 ppm (McLennan, 1989). REE patterns of the ferruginous sedimentary rocks normalized to PAAS show that many Group

A samples have distinct positive Eu anomalies, particularly for those with lower ΣREE concentrations (Fig. 4a). Many Group A samples also have either positive or negative Ce anomalies. In contrast, the REE patterns of Group B and C samples have slightly positive or no Eu anomalies, and many of these samples have prominent negative or positive Ce anomalies (Fig. 4b).

The chemical compositions of the sulfide ores are distinctive, reflecting the ore type. Black ores are generally enriched in Zn (18–39 wt.%), and contain variable amounts of Pb (0.9–12 wt.%) and Cu (0.4–30 wt.%; Supplementary Table 3). The Fe contents of the black ores are also variable (0.2–18 wt.%). The yellow and pyrite ores have much higher Fe contents (ca. 45 wt.%) as compared with the black ores.

4.3. Fe isotopes

δ^{56}Fe values of the ferruginous sedimentary rock samples exhibit a wide variation of ca. 4‰ (–1.75‰ to +2.00‰; Supplementary Table 4; Fig. 5a). The δ^{56}Fe values of many samples are significantly fractionated from that of dissolved Fe in typical high-temperature, seafloor hydrothermal fluids (-0.7 to -0.1‰; Sharma et al., 2001; Severmann et al., 2004; Rouxel et al., 2008) and Fe in igneous and clastic sedimentary rocks (-0.1 to +0.4‰; Dauphas et al., 2017). Group A ferruginous sedimentary rock samples from the Doyashiki (DY), Kosaka (KS), and Matsumine (MT) deposits tend to have lower δ^{56}Fe values (–1.57‰ to +0.20‰), as compared with those from the Ezuri and Fukazawa deposits (–0.49‰ to +2.00‰). Many Group B samples, which formed during post-Kuroko hydrothermal activity, also have fractionated Fe isotopes, with both positive and negative values (–1.75‰ to +0.69‰). The Group C samples of the younger sedimentary rocks have a small range of δ^{56}Fe values (–0.52‰ to +0.11‰).

Analyses of sulfide ores in the Matsumine and Fukazawa deposits showed that the Zn-rich black ores have low δ^{56}Fe values (as low as –1.78‰), whereas the Cu-rich yellow ores have values of ca. –0.5‰, similar to those of dissolved Fe in seafloor hydrothermal fluids (Fig. 5b). No significant difference in sulfide δ^{56}Fe values was observed between the Matsumine and Fukazawa deposits.

5. Discussion

5.1. Sedimentary environments during and after the formation of the Kuroko VMS deposits

Many of the ferruginous sedimentary rock samples examined in this study contain chemical (i.e., authigenic) precipitates, such as microcrystalline quartz and hematite, as well as Mn-bearing minerals (Fig. 2). However, some samples also contain clastic components. This is consistent with a previous study that investigated the mineralogy and geochemistry of ferruginous sedimentary rocks associated with a Kuroko VMS deposit (i.e., Fukazawa) in the Hokuroku region (Kalogeropoulos and Scott, 1983). Petrographic observations show that Mn is hosted not only by Mn oxides, but also by carbonate and silicate phases. However, the carbonate and silicate phases were likely formed by reduction of Mn oxides during sediment burial. Although Mn and other associated trace elements could have been lost during these mineral transformations, the following discussion indicates that the samples preserve geochemical signatures inherited from fluids or generated during precipitation.

Iron and Mn oxides can be used to identify the sedimentary environment of their formation, as these phases sequester trace elements from seawater and/or hydrothermal fluids via adsorption or co-precipitation (German et al., 1990; Bau, 1999; Ohta et al.,

1999). For example, the REE patterns of the ferruginous sedimentary rock samples have non-flat patterns when normalized to PAAS (Fig. 4). This indicates that significant amounts of REEs were chemically added to the sediments during their deposition. A trend of heavy REEs enrichment relative to light REEs, and Ce and Eu anomalies, are typical of some Precambrian BIFs (Planavsky et al., 2010), suggesting that adsorption onto Mn oxides contributed as the additional input of REEs into both the BIFs and ferruginous sedimentary rocks in this study (Ohta and Kawabe, 2001). However, samples that have a high ΣREE concentration are more affected by clastic components, as indicated by a positive trend between ΣREE and Ti concentrations (Fig. S1a). Therefore, the geochemical signatures reflecting seawater or hydrothermal fluids are most prominent in the samples with lower ΣREE concentrations (Fig. 3).

Marked positive Eu anomalies were observed in the ferruginous sedimentary rocks, particularly those of Group A (Figs 4a and 6a), which are indicative of a high-temperature (>250°C) hydrothermal fluid. Such fluids have a distinct positive Eu anomaly due to breakdown of Eu-rich plagioclase during fluid–rock interactions (German et al., 1990; Mills and Elderfield, 1995). No clear correlation was observed between Ba/Eu concentration ratios and Eu anomalies (Fig. S1b), indicating that the Eu anomalies are not an analytical artifact. The positive Eu anomalies in Group A samples are also consistent with their direct or close association with the Kuroko VMS deposits. Although Ohmoto (1996) suggested that most ferruginous cherts associated with VMS deposits were formed from a low-temperature fluid (<150°C), our study suggests that these cherts may have formed from a high-temperature (>250°C) hydrothermal fluid at the same time as sulfide ore formation. Group B samples also show positive Eu anomalies, indicating that they also likely formed from a hydrothermal fluid. However, the Eu anomalies in

405 Group B samples are much smaller than those in Group A samples, suggesting formation
406 from either a lower temperature fluid or that with a smaller input of hydrothermal fluid
407 as compared with Group A samples. This further implies that higher temperature fluids
408 or greater hydrothermal activity was required for the formation of the Kuroko VMS
409 deposits. Positive Eu anomalies in exhalates have also been reported for other VMS
410 deposits (e.g., Miller et al., 2001; Grenne and Slack, 2005; Slack et al., 2007; Slack et al.,
411 2009). Grenne and Slack (2005) estimated that even 0.03%–0.1% of a contribution from
412 hydrothermal fluid is enough to develop a positive Eu anomaly in exhalates, if the
413 hydrothermal fluid has a distinctive positive Eu anomaly, such as those at the TAG site
414 on the Mid-Atlantic Ridge (Mills and Elderfield, 1995).

415 Positive and negative Ce anomalies characterize many Group A and B samples
416 (Fig. 4). The negative Ce anomalies indicate that the REEs were also sequestered from
417 oxygenated seawater in addition to hydrothermal fluids, because REE patterns of
418 oxygenated seawater have a distinct negative Ce anomaly due to preferential removal of
419 Ce into marine sediments (Byrne and Sholkovitz, 1996). Negative Ce anomalies are also
420 observed for samples with high ΣREE and Ti concentrations (Fig. S2a), which might
421 indicate that the anomalies resulted from later alteration or oxidation during weathering
422 (e.g., Hayashi et al., 2004), particularly in the case of samples collected from outcrops
423 (i.e., Groups B and C). However, Group A samples should not have been affected by
424 weathering, because they were obtained from underground mines. In addition, positive
425 Ce anomalies tend to be found in Mn-rich samples in both Group A and B samples (Fig.
426 6b). Because Mn oxides promote oxidation of Ce^{3+} to insoluble Ce^{4+}, ferromanganese
427 nodules in modern oceans bear positive Ce anomalies (Ohta et al., 1999; Ohta and
428 Kawabe, 2001) regardless that REEs are adsorbed from oxygenated seawater with a

429 distinct negative Ce anomaly. Therefore, positive Ce anomalies in Mn-rich samples in the
430 Hokuroku basin suggest that Mn oxides were primarily precipitated from oxygenated
431 seawater. Although the mineralogy of the Mn-rich samples was modified during
432 diagenesis, as indicated by petrographic observations, the Ce anomalies were likely
433 inherited from seawater or generated during chemical precipitation of the sediments (Kato
434 et al., 2006). An apparent Ce anomaly might result from a positive La anomaly; however,
435 on a Ce anomaly vs. Pr anomaly diagram (Bau and Dulski, 1996) almost all the samples
436 have true (i.e., not apparent) positive or negative Ce anomalies (Fig. S2b).

437 Large Fe isotope variations (–1.75‰ to +2.00‰) were observed in the ferruginous
438 sedimentary rocks from Groups A and B (Fig. 5). This range is as large as the Fe isotope
439 variations of oxide phases (i.e., hematite and magnetite) in BIFs throughout Earth's
440 history (~-2.5 to ~+2‰; Dauphas et al., 2017), indicating that Fe was enriched in the
441 studied samples by chemical precipitation during sedimentation. Furthermore, the large
442 Fe isotope variations are indicative of Rayleigh-type fractionation associated with partial
443 oxidation of dissolved Fe^{2+} derived from hydrothermal fluids. The partial oxidation
444 occurred by mixing of hydrothermal fluids with oxygenated seawater, which is supported
445 by the observation that many samples with fractionated $\delta^{56}Fe$ values also have negative
446 Ce anomalies (Fig. 7a). If the partial oxidation occurred in a completely oxygenated open
447 ocean, then $\delta^{56}Fe$ values would shift to negative values with increasing Mn/Fe ratios,
448 because of the difference in the oxidation rate of Mn^{2+} and Fe^{2+} that has been observed in
449 ferromanganese sediments in recent marine hydrothermal systems (e.g., Chu et al., 2006;
450 Rouxel et al., 2018). However, the samples in the present study do not show a correlation
451 between $\delta^{56}Fe$ values and Mn/Fe ratios (Fig. 7b), indicating that the geochemical behavior
452 of Mn and Fe was decoupled.

Our whole-rock Fe isotope data for the ferruginous sedimentary rocks could have been affected by Fe derived from clastic materials or sulfide minerals present in the samples, and not solely reflect chemically precipitated Fe oxides. However, because the Fe from the clastic materials should have $\delta^{56}Fe \sim 0‰$, similar to igneous or clastic sedimentary rocks (Dauphas et al., 2017), this would only reduce the $\delta^{56}Fe$ variations. Although no clear trend between the abundance of sulfide minerals and $\delta^{56}Fe$ values was observed, sulfide minerals (e.g., pyrite) may have $\delta^{56}Fe$ values that are lower than hematite (Rouxel et al., 2004; Rouxel et al., 2008), which could affect the whole-rock Fe isotope data. Bennett et al. (2009) reported that the difference between Fe-sulfide and Fe-oxyhydroxide ($\Delta^{56}Fe_{Fe\text{-}sulfide–Fe\text{-}oxyhydroxide}$) in the same hydrothermal plume was -0.70‰. Therefore, we evaluated the effects of pyrite on the whole-rock Fe isotope data in some relatively pyrite-rich samples by analyzing the Fe isotope compositions of pyrite and hematite that were handpicked from crushed samples. The results show that the whole-rock Fe isotope compositions of most samples are close to that of hematite, whereas $\delta^{56}Fe$ values of pyrite were either lower or higher than that of hematite (Fig. S3). In addition, because pyrite contents were low in most samples, the whole-rock Fe isotope compositions can be assumed to approximate that of hematite. Bacterial iron reduction during burial of the sediments could have also significantly altered the Fe isotope signature (e.g., Yamaguchi et al., 2005). However, organic matter contents were likely very low in these samples, and no evidence of reduction of iron oxides (e.g., formation of magnetite or siderite) was observed. Although some of the ferruginous sedimentary rocks may have been subjected to weathering in the outcrops, this is unlikely to have significantly altered the whole-rock Fe isotope compositions because Fe^{3+} has limited mobility in oxidized environments. Therefore, the $\delta^{56}Fe$ values of the ferruginous

sedimentary rocks studied here most likely reflect the primary signature when Fe (hydr)oxides were chemically precipitated due to mixing of hydrothermal fluids and seawater.

δ^{56}Fe variations observed in the ferruginous sedimentary rocks can be modeled using two-step Rayleigh-type fractionation (e.g., Moeller et al., 2014), in which Fe isotope fractionation during oxidative precipitation of dissolved Fe^{2+} is explained by the following processes (e.g., Beard and Johnson, 2004; Dauphas and Rouxel, 2006):

$$Fe^{2+}_{(aq)} \leftrightharpoons Fe^{3+}_{(aq)} \rightarrow Fe^{3+}(s) \quad (4),$$

where an equilibrium isotope effect occurs in the first step between aqueous ferrous iron ($Fe^{2+}_{(aq)}$) and ferric iron ($Fe^{3+}_{(aq)}$) and a kinetic isotope effect occurs in the second step during precipitation of ferric iron ($Fe^{3+}_{(s)}$) from $Fe^{3+}_{(aq)}$. The overall isotope effects are determined by rate constants (k_1 and k_2) and fractionation factors (α_1 and α_2) governed by temperature in both steps. We assumed that the ferruginous cherts were precipitated at ca. 100°C, based on the oxygen isotope study of Tsutsumi and Ohmoto (1983), and used +2.0‰ for α_1 (Fujii et al., 2014) and –0.8‰ for α_2 (Skulan et al., 2002). Because no data are available for either k_1 or k_2 at the relevant temperature, we used the values at 25°C (k_1 = 0.0827; k_2/k_1 = 10) from Beard and Johnson (2004). Although k_1 and k_2 should be higher at 100°C than these values, isotopic ratios of each species are not significantly affected by the increase in k_1 and k_2 in the model because k_1 = 0.0827 and k_2/k_1 = 10 are already high enough to quickly reach the steady state concentrations.

The results of our model calculations in both open and closed systems using the above parameters show that the model, particularly in an open system, can explain the Fe isotope variations observed in most Group A and B samples with negative shifts in δ^{56}Fe when the initial δ^{56}Fe value for $Fe^{2+}_{(aq)}$ was assumed to be –0.5‰ (e.g., Rouxel et al.,

501 2008; Fig. 8a). Furthermore, the model can explain the positive shifts in $\delta^{56}Fe$ values as
502 observed in the Ezuri and Fukazawa deposits (Fig. 5a), if the initial $\delta^{56}Fe$ value of $Fe^{2+}_{(aq)}$
503 was as high as +0.5‰ (Fig. 8b). Therefore, we suggest that the initial $\delta^{56}Fe$ value of
504 $Fe^{2+}_{(aq)}$ was +0.5‰, possibly due to the precipitation of pyrite in black ores during the
505 formation of the ferruginous cherts in the Ezuri and Fukazawa deposit (see section 5.2).

506 Note that the temperature at which $Fe^{3+}_{(s)}$ precipitated (i.e., 100°C) may not be
507 accurately estimated. Tsutsumi and Ohmoto (1983) assumed the isotopic equilibrium
508 between hematite and quartz to estimate the formation temperature of the ferruginous
509 cherts. However, they can be in a disequilibrium assemblage or reset by recrystallization
510 during diagenesis. Then, the temperature at which $Fe^{3+}_{(s)}$ precipitated may have been
511 lower than 100°C. Whereas temperature dependency of Fe isotope effect during oxidative
512 precipitation of $Fe^{2+}_{(aq)}$ is not well understood, the overall isotope effect can be relatively
513 constant at variable temperatures due to offsetting changes in α_1 and α_2 values. In the case
514 that α_1 is more sensitive than α_2 to the temperature change as implied by Skulan et al.
515 (2002) and Beard et al. (2010), the overall isotope effect would have been larger at a lower
516 temperature, which makes the model more feasible to explain the observed variation in
517 $\delta^{56}Fe$ values with a smaller fraction of $Fe^{3+}_{(s)}$.

518 The positive Eu and negative Ce anomalies, and large Fe isotope fractionations
519 that are decoupled from Mn, can be best explained if the seawater was locally redox-
520 stratified at the bottom of the Hokuroku Basin. Partial oxidation of dissolved Fe^{2+} in a
521 hydrothermal fluid likely occurred at the redox interface, at which precipitated iron
522 (hydr)oxides may have sequestered REEs from both hydrothermal fluids and oxygenated
523 seawater (Fig. 9). There is a possibility that the bottom water was suboxic (<5 μmol/l of
524 dissolved O_2 concentration), not completely anoxic. For example, Slack et al. (2007)

propose that late Paleoproterozoic ferruginous cherts and iron formation in Arizona, USA were formed under suboxic conditions, primarily based on REE patterns showing weak positive and negative Ce anomalies. Partial oxidation of $Fe^{2+}_{(aq)}$ derived from hydrothermal fluids under suboxic conditions may have also caused a large Fe isotope fractionation with decoupling Fe and Mn behaviors.

The extent of Fe isotope fractionation was likely determined by the balance between the hydrothermal influx and outflux to the sink. If the hydrothermal Fe influx or reserves in a pool were large enough to maintain a relatively constant dissolved Fe concentration and isotopic composition, then heavy $\delta^{56}Fe$ values (e.g., ca. +0.5‰) with minimal variation would be expected for the precipitated iron (hydr)oxides due to the isotope effects during oxidative precipitation of dissolved Fe^{2+} (e.g., ~+1‰; Bullen et al., 2001; Beard et al., 2010). However, Rayleigh-type fractionation was recognized in the present study, suggesting that the Fe influx from hydrothermal fluids was rather limited. We also suggest that the anoxic or suboxic pools were not large enough to maintain a constant Fe isotopic composition, possibly due to these representing local depressions in the Hokuroku Basin. Decoupling of Mn and Fe suggests that Mn oxides were mostly dissolved in the anoxic or suboxic pools, although they may have also formed at the redox interface (Fig. 9). Mn oxides preserved in the Mn-rich samples were probably formed at the edges of the depressions that were in oxidized environments. Most Mn-rich (i.e., high Mn/Fe ratio) samples have positive Ce anomalies due to selective oxidation of Ce^{3+} to Ce^{4+} in oxidized conditions (Ohta and Kawabe, 2001).

The localized anoxic or suboxic pools may have had an important role in the preservation of the sulfide ores that were exposed to the seafloor, as otherwise these would have been oxidized and dissolved (or transformed into iron hydroxides). However,

549 our Fe isotope data indicate that the anoxic or suboxic pools were also present during
550 post-Kuroko hydrothermal activity when Group B samples were deposited, because their
551 Fe isotope variations are as large as those in Group A (Fig. 5). Therefore, redox
552 stratification at the bottom of the Hokuroku Basin persisted for a significant period of
553 time (ca. 3 Myr), even though the Kuroko VMS deposits were only formed in one
554 particular stratigraphic interval. This was probably due to differences in the intensity of
555 hydrothermal activity, as highlighted by the marked Eu anomalies of Group A samples.
556 Fe isotope data in Group C suggests that the Hokuroku basin became completely oxic
557 because Fe oxides in the samples inherited the isotope compositions of $Fe^{2+}_{(aq)}$ in
558 hydrothermal fluids (i.e., ~-0.5‰) by quantitative oxidation. Although it is possible that
559 the narrow range in the $\delta^{56}Fe$ values is caused by sampling bias due to the limited sample
560 number in Group C (n = 5), the geochemical trends are consistent with the geological
561 history, in which the Hokuroku basin became shallower associated with uplifting the
562 region starting ~12 Ma (Yamada and Yoshida, 2011).
563
564 5.2. Sulfide ore formation processes inferred from Fe isotopes
565 $\delta^{56}Fe$ values of most Group A samples, which are associated with the Kuroko
566 VMS deposits, are shifted to negative values, whereas those from the Fukazawa and Ezuri
567 deposits are shifted to positive values (Fig. 5a). These differences may provide insights
568 into the formation of the ore bodies or physicochemical conditions of the mineralizing
569 fluids. These differences are also evident from the observation that the Fukazawa and
570 Ezuri deposits are located in the central area of the Hokuroku Basin, and that the
571 Fukazawa deposit contains only a small amount of yellow ore. Iron isotope data for
572 sulfide ores from the Fukazawa and Matsumine deposits are similar, and the black ores

have lower ^{56}Fe values than the yellow and pyrite ores (Fig. 5b). The negative $\delta^{56}Fe$ values of the black ores likely reflect rapid precipitation of pyrite. Syverson et al. (2013) experimentally demonstrated that a kinetic isotope effect (ca. –0.5‰) on Fe isotopes (i.e., $\delta^{56}Fe$) occurs during the initial precipitation of pyrite at 300–350°C. This kinetic isotope effect could be even larger at the lower temperatures at which the black ores were formed (e.g., 150–300°C; Ohmoto, 1996), when pyrite was rapidly precipitated by mixing with seawater. The black ores comprise fine-grained pyrite that is intergrown with sphalerite and galena (Fig. 2e), which also indicates the rapid precipitation of the sulfides. Iron isotope analysis of sulfide deposits and chimneys in modern hydrothermal systems have also shown that Zn-rich sulfides tend to be depleted in ^{56}Fe (Rouxel et al., 2008; Li et al., 2018b), which is consistent with the results of this study.

However, petrographic observations of the yellow and pyrite ores (Fig. 2f) suggest that they likely formed by slow growth of pyrite from a high-temperature hydrothermal fluid. This is consistent with the replacement growth model for Kuroko-type VMS deposits (Ohmoto, 1996), in which yellow ores formed by replacing black ores during the growth of the ore bodies. $\delta^{56}Fe$ values of the yellow and pyrite ores have a narrow range (–0.59‰ to –0.26‰; Fig. 5b), almost identical to the range of $\delta^{56}Fe$ values of dissolved Fe in typical seafloor hydrothermal fluids (Sharma et al., 2001; Severmann et al., 2004; Rouxel et al., 2008). We suggest that pyrite in the yellow and pyrite ores exchanged Fe isotopes with mineralizing hydrothermal fluids toward their isotopic equilibrium. Syverson et al. (2013) experimentally estimated that the equilibrium fractionation factor between pyrite and aqueous Fe in a fluid ($\Delta^{56}Fe_{py–Fe(aq)}$) was +0.99‰ at 350°C. The smaller isotope fractionation between Fe in the ores and fluids suggests that the isotopic equilibrium was not attained. Given that Fe in the ores is partly hosted

by chalcopyrite, which has a smaller fractionation factor with aqueous Fe in a fluid ($\Delta^{56}Fe_{ccp}$-$Fe_{(aq)}$ = 0.09‰; Syverson et al., 2017), this may have also contributed to the lower $\delta^{56}Fe$ values of the yellow ores.

As such, the similarity in the Fe isotope signatures of the black and yellow ores in the Matsumine and Fukazawa deposits suggests that the ore-forming processes were basically the same. Therefore, the difference in the abundance of yellow ores in the two deposits likely reflects variable durations of hydrothermal circulation at the two sites. For the Matsumine deposit, long-term hydrothermal activity may have facilitated the development of a large yellow ore body (Fig. 10a). Based on numerical simulations, Schardt and Large (2009) suggested that an average VMS deposit (e.g., Fukazawa) may take ca. 5 kyr to form, whereas the formation of a large Cu-rich VMS deposit (e.g., Matsumine) may require a longer time (>35 kyr) and higher maximum temperature (>300°C). The overlying ferruginous sedimentary rocks may have precipitated from the hydrothermal fluid responsible for the formation of the yellow ores, or later during the waning stages of hydrothermal activity when the $\delta^{56}Fe$ values of dissolved Fe in the hydrothermal fluid were ca. –0.5‰. The prominent Eu anomalies in the ferruginous sedimentary rocks associated with the Kuroko VMS deposits (Fig. 4a) suggest that the former is more likely, since it indicates high-temperature (e.g., 250°C) hydrothermal activity. The negative $\delta^{56}Fe$ values of the ferruginous sedimentary rocks in the Matsumine deposit (Fig. 5a) can be explained by the partial oxidation of dissolved Fe at the redox interface in an anoxic or suboxic pool. The sulfide ore body exposed at the seafloor could then have been preserved.

In contrast, for the Fukazawa deposit, the hydrothermal fluids that formed the overlying ferruginous cherts were likely responsible for the formation of black ores. In

621 this deposit, the $\delta^{56}Fe$ values in the hydrothermal fluids, affected by the kinetic isotope
622 effect during pyrite formation in black ores, were shifted to a more positive value (ca.
623 +0.5‰). Therefore, iron oxides precipitated from the hydrothermal fluids were also
624 shifted to more positive $\delta^{56}Fe$ values (Figs 5b and 8b). The Fukazawa deposit is
625 characterized by abundant black ores relative to yellow ores, suggesting that
626 hydrothermal circulation was not protracted or intense enough to develop yellow ores
627 (Fig. 10b). Localized anoxic pools may or may not have been present at the depositional
628 site of the Fukazawa deposit, because hydrothermal circulation was short (ca. 5 kyr) and
629 the ores were quickly buried by erupted basaltic lava flows (Fig. 1).
630
631 5.3. Implications of this study
632 The results of this study suggest that a local anoxic or suboxic water column is
633 an important factor for preserving sulfide ores in VMS deposits formed on the seafloor in
634 back-arc settings. However, it is not the only factor, because the local redox stratification
635 was persistent at the bottom of the Hokuroku Basin until post-Kuroko hydrothermal
636 activity, as indicated by the large Fe isotope fractionations in the younger sedimentary
637 rocks (Fig. 5a). The most significant geochemical difference in the ferruginous
638 sedimentary rocks associated with the Kuroko VMS deposits as compared with those
639 formed later is the presence of marked positive Eu anomalies (Fig. 4a; Fig. 6a), which are
640 indicative of a high-temperature hydrothermal fluid. Therefore, in addition to the
641 presence of localized anoxic or suboxic pools, high-temperature hydrothermal activity is
642 a prerequisite for VMS ore deposit formation. Therefore, large Fe isotope variations
643 coupled with positive Eu anomalies in ferruginous sedimentary rocks can be used as an
644 indicator and exploration tool for underlying VMS ore mineralization. However, it is

important to note that not all samples associated with the Kuroko VMS deposits exhibit large Fe isotope fractionations or positive Eu anomalies. This may be due to contamination by detrital components or the distance from the sulfide ore bodies and source of the hydrothermal fluids.

Another important finding from this study is the large Fe isotope fractionations in massive sulfide ores, particularly in the Zn-rich black ores (Fig. 5b). Although some recent studies have also analyzed the Fe isotope compositions of sulfide ores and minerals in other types of ore deposits (e.g., He et al., 2020), the documented variations in δ^{56}Fe values are usually between –1‰ and +1‰, and not as large as that found in this study. This is because the Kuroko-type VMS deposits, and particularly the black ores, were formed by dynamic mixing of hydrothermal fluids with seawater. A large Fe isotope variation was also identified in the Navan Zn–Pb Irish-type deposit (Gagnevin et al., 2012), which can be classified as a hybrid MVT–SEDEX deposit. Therefore, the results of our study warrant further investigation on the Fe isotope compositions of sulfide minerals formed in ore deposits by similar submarine hydrothermal processes (e.g., other types of VMS, SEDEX, and sediment-hosted Cu deposits).

6. Conclusions

We investigated the petrographic and geochemical characteristics and stable Fe isotope systematics of ferruginous sedimentary rocks in Kuroko VMS deposits, as well as younger sedimentary rocks in the Hokuroku Basin, northeast Japan. The Fe isotope compositions of sulfide ores in two representative Kuroko VMS deposits (Matsumine and Fukazawa) were also investigated to understand the ore formation processes and genetic links between the ferruginous sedimentary rocks and sulfide ore bodies. Our main

669 findings are summarized below:

670 • The ferruginous sedimentary rocks have variable Fe_2O_3, MnO, and SiO_2 contents.
671 Although some samples contain clastic components, these rocks consist
672 predominantly of precipitates formed by mixing of hydrothermal fluids and seawater.
673 Therefore, REE patterns and Fe isotope compositions reflect the geochemical state
674 of the hydrothermal fluid and seawater, as well as the sedimentary environments.

675 • Ferruginous sedimentary rocks associated with the Kuroko VMS deposits tend to
676 have prominent positive Eu anomalies, which indicate formation associated with a
677 high-temperature hydrothermal fluid. Many of the ferruginous sedimentary rocks
678 deposited during and after Kuroko VMS ore deposit formation have negative or
679 positive Ce anomalies, which indicate mixing with oxygenated seawater and/or
680 precipitation of MnO_2 during the deposition of these rocks.

681 • Large Fe isotope variations ($\delta^{56}Fe$ = –2‰ to +2‰) and deviations from the expected
682 $\delta^{56}Fe$ values (ca. –0.5‰) of dissolved Fe in typical seafloor hydrothermal fluids
683 were observed in the ferruginous sedimentary rocks deposited during and after
684 Kuroko VMS ore deposit formation. This suggests that iron (hydr)oxides were
685 precipitated by the partial oxidation of dissolved Fe^{2+} derived from a hydrothermal
686 fluid in a redox-stratified water column, although anoxic or suboxic pools are likely
687 to have occurred locally in the Hokuroku Basin. The anoxic or suboxic pools may
688 have been an important factor for preservation of the sulfide ore bodies on the
689 seafloor.

690 • $\delta^{56}Fe$ values in ferruginous sedimentary rocks from the Fukazawa and Ezuri deposits
691 have heavier values of up to +2.00‰. This can be explained by simultaneous
692 precipitation of sulfide ores and deposition of ferruginous sedimentary rocks,

693 whereby the $\delta^{56}Fe$ values of the hydrothermal fluids were shifted to positive values
694 (ca. +0.5‰) by a kinetic isotope effect during rapid precipitation of pyrite.

695 • Iron isotope analysis of the sulfide ores in the yellow ore-rich Matsumine deposit
696 and black ore-rich Fukazawa deposit showed that the Zn-rich black ores are
697 isotopically lighter and the Cu-rich yellow ores are isotopically similar to the
698 hydrothermal fluids. No significant difference in $\delta^{56}Fe$ values was observed between
699 the two deposits. The black ores likely formed by rapid precipitation of sulfide
700 minerals due to the mixing of hydrothermal fluids and seawater. The yellow ores
701 likely formed by slow growth of pyrite from high-temperature hydrothermal fluids
702 that replaced black ores during the growth of the Kuroko VMS ore deposit. The
703 difference in the abundance of yellow sulfide ores between the two deposits may
704 reflect variable durations of hydrothermal circulation.

705 In summary, Fe isotope systematics of sulfide ores and overlying ferruginous
706 sedimentary rocks in Kuroko-type VMS deposits can reveal the geochemical nature of
707 the mineralizing hydrothermal fluids and seawater, as well as the ore formation processes.
708

709 **Acknowledgements**

710 We thank DOWA Metal & Mining Co., Ltd. for providing the samples and
711 information regarding the ore reserves, and A. Matsumoto for technical assistance with
712 the XRF analysis. We also thank O. Rouxel for the editorial handling as well as D.
713 Syverson and two anonymous reviewers for their constructive comments on the
714 manuscript. This research was supported by a Joint Research Grant for an Environmental
715 Isotope Study of the Research Institute for Humanity and Nature, Next-Generation
716 Technology for Ocean Resources Exploration Project from the Cross-Ministerial

717 Strategic Innovation Promotion Program (SIP) of the Japanese Cabinet Office, the Japan
718 Mining Industry Association (JMIA), and Japan Society for the Promotion of Science
719 (JSPS) KAKENHI Funds (26709069, 17H03502, 20H00184) to T.O.

720

721 **Appendix A. Supplementary Material**

722 Supplementary data to this article can be found online at https://doi.org/xxxxxxxxxxxxxx.

723

Figure Captions

Figure 1. Stratigraphy of the Hokuroku district (after Yamada et al., 2012). P = phyllite and chert basement; G = granitic rock; A5 = andesite lava flow, tuff breccia, and sandstone; B2 and B3 = pillow basalt, diabase sill, and basaltic tuff; M1–M3 = mudstone; T1–T4 = tuff (pumiceous tuff and tuff breccia) and volcanic breccia; R1–R4 = rhyolite. The ore horizon of Kuroko-type VMS mineralization occurs in the T3 tuff just below the M2a mudstone. Ferruginous sedimentary rock samples were taken from: DY = Doyashiki; MT = Matsumine; EZ = Ezuri; FZ = Fukazawa; KS = Kosaka; NT = Nittobe; NR = Nagatoro; KY = Koyukisawa; SN = Shinekari; DM = Daimyojin.

Figure 2. Photomicrographs of ferruginous sedimentary rock and massive sulfide ore samples. (a) EZ4: ferruginous chert composed predominantly of microcrystalline quartz and hematite (XP; ×100); (b) KS3: barite-rich sample from the Kosaka deposit that is directly associated with massive sulfide ore (XP; ×50); (c) KS2: ferruginous chert containing some detrital materials from the Kosaka deposit (XP; ×100); (d) MT3: ferromanganese sample from the Matsumine deposit, consisting of alternating ferruginous and ferromanganese layers (XP; ×50); (e) FZ53: representative black ore (Zn–Pb-rich) from the Fukazawa deposit (RL; ×100); (f) MT54: representative yellow ore (Cu–Fe-rich) from the Matsumine deposit (RL; ×50). Hm = hematite; QZ = quartz; Br = barite; Py = pyrite; Cp = chalcopyrite; Mn–Ca-carb = Mn–Ca carbonates; Gt = goethite; Ms = muscovite; Pg = plagioclase; Qt(d) = detrital quartz; Gn = galena; Sp = sphalerite; Th = tetrahedrite; XP = cross-polarized transmitted light; RL = reflected light.

748 **Figure 3**. Box plots of (a) Fe_2O_3, (b) Al_2O_3, and (c) MnO contents in Group A samples
749 (associated with VMS deposits), and Group B and C samples (not associated with VMS
750 deposits). Samples that were below XRF detection limits for Al_2O_3 (<0.05 wt.%) were
751 excluded from (b).
752
753 **Figure 4**. Rare earth element (REE) patterns normalized to Post-Archean Australian
754 Shale (PAAS; McLennan, 1989) for (a) Group A samples (associated with VMS deposits)
755 and (b) Group B and C samples (not associated with VMS deposits).
756
757 **Figure 5**. $\delta^{56}Fe$ values of (a) ferruginous sedimentary rock samples plotted according to
758 their stratigraphy and (b) sulfide ores from the Matsumine and Fukazawa deposits. Gray
759 shaded areas indicate the $\delta^{56}Fe$ range for typical high-temperature, seafloor hydrothermal
760 fluids (Sharma et al., 2001; Severmann et al., 2004; Rouxel et al., 2008). DY = Doyashiki;
761 MT = Matsumine; EZ = Ezuri; FZ = Fukazawa; KS = Kosaka; NT = Nittobe; NR =
762 Nagatoro; KY = Koyukisawa; SN = Shinekari; DM = Daimyojin.
763
764 **Figure 6**. Plots of the (a) Eu anomaly (Eu/Eu*) vs. Ti concentration and (b) Ce anomaly
765 (Ce/Ce*) vs. Mn concentration for the ferruginous sedimentary rock samples.
766
767 **Figure 7**. Plots of the (a) Ce anomaly (Ce/Ce*) and (b) Mn/Fe ratios vs. $\delta^{56}Fe$ values for
768 the ferruginous sedimentary rock samples. Gray shaded areas on the x-axis indicate the
769 $\delta^{56}Fe$ range for typical high-temperature, seafloor hydrothermal fluids (Sharma et al.,
770 2001; Severmann et al., 2004; Rouxel et al., 2008).
771

772 **Figure 8**. Rayleigh-type model calculations for $\delta^{56}Fe$ values of precipitated ferric
773 hydroxides from a $Fe^{2+}_{(aq)}$-bearing fluid as a function of the fraction of precipitated ferric
774 iron ($Fe^{3+}_{(s)}$), assuming that the initial $\delta^{56}Fe$ value of Fe in the fluid is (a) –0.5‰ and (b)
775 +0.5‰. The measured $\delta^{56}Fe$ range for most samples in Groups A and B are plotted in (a),
776 whereas that for the Ezuri and Fukazawa deposits in Group A is plotted in (b). See the
777 main text for description of the model and estimates of the parameters, including the
778 isotope fractionation factors.
779
780 **Figure 9**. Schematic diagram to illustrate geochemical behaviors of Fe and Mn as well as
781 rare earth element (REE) signatures in a redox-stratified seawater. +Eu/Eu*, +Ce/Ce*,
782 and -Ce/Ce* indicate positive Eu, positive Ce, and negative Ce anomalies, respectively.
783 Ads. is an abbreviation for adsorption.
784
785 **Figure 10**. Schematic diagram of the formation processes of sulfide ore bodies and
786 ferruginous sedimentary rocks in the (a) Matsumine and (b) Fukazawa deposits.
787
788 **References**
789
790 Bau M. and Dulski P. (1996) Distribution of yttrium and rare-earth elements in the Penge
791 and Kuruman iron-formations, Transvaal Supergroup, South Africa. *Precambrian*
792 *Res.* **79**, 37-55.

793 Bau M. (1999) Scavenging of dissolved yttrium and rare earths by precipitating iron
794 oxyhydroxide: Experimental evidence for Ce oxidation, Y-Ho fractionation, and
795 lanthanide tetrad effect. *Geochim. Cosmochim. Acta* **63**, 67-77.

796 Beard B. L. and Johnson C. M. (1999) High precision iron isotope measurements of
797 terrestrial and lunar materials. *Geochim. Cosmochim. Acta* **63**, 1653-1660.

798 Beard B. L. and Johnson C. M. (2004) Fe isotope variations in the modern and ancient
799 Earth and other planetary bodies. In *Geochemistry of Non-tradtional Stable*
800 *Isotopes* (eds. C. M. Johnson, B. L. Beard and F. Albarède). Mineralogial Society
801 of America, Washington, DC, pp. 319-357.

802 Beard B. L., Handler R. M., Scherer M. M., Wu L., Czaja A. D., Heimann A. and Johnson
803 C. M. (2010) Iron isotope fractionation between aqueous ferrous iron and goethite.
804 *Earth. Planet. Sci. Lett.* **295**, 241-250.

805 Bennett S. A., Rouxel O., Schmidt K., Garbe-Schönberg D., Statham P. J. and German C.
806 R. (2009) Iron isotope fractionation in a buoyant hydrothermal plume, 5°S Mid-
807 Atlantic Ridge. *Geochim. Cosmochim. Acta* **73**, 5619-5634.

808 Borrok D. M., Wanty R. B., Ridley W. I., Wolf R., Lamothe P. J. and Adams M. (2007)
809 Separation of copper, iron, and zinc from complex aqueous solutions for isotopic
810 measurement. *Chem. Geol.* **242**, 400-414.

811 Bullen T. D., White A. F., Childs C. W., Vivit D. V. and Schulz M. S. (2001)
812 Demonstration of significant abiotic iron isotope fractionation in nature. *Geology*
813 **29**, 699-702.

814 Byrne R. H. and Sholkovitz E. R. (1996) Marine chemistry and geochemistry of the
815 lanthanides. In *Handbook on the Physics and Chemistry of Rare Earths* (eds. K.
816 A. Gschneider Jr. and L. Eyring). Elsevier, Amsterdam, pp. 497-593.

817 Chu N.-C., Johnson C. M., Beard B. L., German C. R., Nesbitt R. W., Frank M., Bohn
818 M., Kubik P. W., Usui A. and Graham I. (2006) Evidence for hydrothermal venting
819 in Fe isotope compositions of the deep Pacific Ocean through time. *Earth. Planet.*
820 *Sci. Lett.* **245**, 202-217.

821 Condie K. C. (1993) Chemical composition and evolution of the upper continental crust:
822 Contrasting results from surface samples and shales. *Chem. Geol.* **104**, 1-37.

823 Cox D. P. and Singer D. A. (1986) *Mineral deposit models*. *U.S. Geological Survey*
824 *Bulletin* **1693**, U.S. Geological Survery, Denver, CO, 379 pp.

825 Dauphas N. and Rouxel O. (2006) Mass spectrometry and natural variations of iron
826 isotopes. *Mass Spectrom. Rev.* **25**, 515-550.

827 Dauphas N., John S. G. and Rouxel O. (2017) Iron isotope systematics. In *Non-traditional*
828 *Stable Isotopes* (eds. F.-Z. Teng, J. M. Watkins and N. Dauphas). Mineralogical
829 Society of America, Chantilly, VA, pp. 415-510.

830 Eldridge C. S., Barton P. B. and Ohmoto H. (1983) Mineral textures and their bearing on
831 formation of the Kuroko orebodies. In *The Kuroko and Related Volcanogenic*
832 *Massive Sulfide Deposits* (eds. H. Ohmoto and B. J. Skinner). Economic Geology
833 Publishing Company, New Haven, CT, pp. 241-281.

834 Franklin J. M., Lydon J. W. and Sangster D. F. (1981) Volcanic-assocaited massive sulfide
835 deposits. In *Economic Geology: Seventy-Fifth Anniversary Volume* (ed. B. J.
836 Skinner). Economic Geology Publishing Company, El Paso, TX, pp. 485-627.

837 Franklin J. M., Gibson H. L., Jonasson I. R. and Galley A. G. (2005) Volcanogenic
838 massive sulfide deposits. In *Economic Geology: One hundredth Anniversary*
839 *Volume* (eds. J. W. Hedenquist, J. F. H. Thompson, R. J. Goldfarb and J. P.

Richards). Society of Economic Geologists, Littleton, CO, pp. 523-560.

Fujii T., Moynier F., Blichert-Toft J. and Albarède F. (2014) Density functional theory estimation of isotope fractionation of Fe, Ni, Cu, and Zn among species relevant to geochemical and biological environments. *Geochim. Cosmochim. Acta* **140**, 553-576.

Gagnevin D., Boyce A. J., Barrie C. D., Menuge J. F. and Blakeman R. J. (2012) Zn, Fe and S isotope fractionation in a large hydrothermal system. *Geochim. Cosmochim. Acta* **88**, 183-198.

German C. R., Klinkhammer G. P., Edmond J. M., Mitra A. and Elderfield H. (1990) Hydrothermal scavenging of rare-earth elements in the ocean. *Nature* **345**, 516-518.

Goodfellow W. D., Peter J. M., Winchester J. A. and van Staal C. R. (2003) Ambient marine environment and sediment provenance during formation of massive sulfide deposits in the Bathurst Mining Camp: Importance of reduced bottom waters to sulfide precipitation and preservation. In *Massive Sulfide Deposits of the Bathurst Mining Camp, New Brunswick, and Northern Maine* (eds. W. D. Goodfellow, S. R. McCutcheon and J. M. Peter). Society of Economic Geologists, Ottawa, ON, pp. 129-156.

Grenne T. and Slack J. F. (2005) Geochemistry of jasper beds from the Ordovician Løkken ophiolite, Norway: Origin of proximal and distal siliceous exhalites. *Econ. Geol.* **100**, 1511-1527.

Günther T., Klemd R., Zhang X., Horn I. and Weyer S. (2017) In-situ trace element and Fe-isotope studies on magnetite of the volcanic-hosted Zhibo and Chagangnuoer iron ore deposits in the Western Tianshan, NW China. *Chem. Geol.* **453**, 111-127.

Hayashi T., Tanimizu M. and Tanaka T. (2004) Origin of negative Ce anomalies in Barberton sedimentary rocks, deduced from La–Ce and Sm–Nd isotope systematics. *Precambrian Res.* **135**, 345-357.

He Z., Zhang X., Deng X., Hu H., Li Y., Yu H., Archer C., Li J. and Huang F. (2020) The behavior of Fe and S isotopes in porphyry copper systems: Constraints from the Tongshankou Cu-Mo deposit, Eastern China. *Geochim. Cosmochim. Acta* **270**, 61-83.

Heimann A., Johnson C. M., Beard B. L., Valley J. W., Roden E. E., Spicuzza M. J. and Beukes N. J. (2010) Fe, C, and O isotope compositions of banded iron formation carbonates demonstrate a major role for dissimilatory iron reduction in ~2.5 Ga marine environments. *Earth. Planet. Sci. Lett.* **294**, 8-18.

Hofmann A., Bekker A., Dirks P., Gueguen B., Rumble D. and Rouxel O. J. (2014) Comparing orthomagmatic and hydrothermal mineralization models for komatiite-hosted nickel deposits in Zimbabwe using multiple-sulfur, iron, and nickel isotope data. *Miner. Deposita* **49**, 75-100.

879 Ito A., Otake T., Shin K.-C., Ariffin K. S., Yeoh F.-Y. and Sato T. (2017) Geochemical
880 signatures and processes in a stream contaminated by heavy mineral processing
881 near Ipoh city, Malaysia. *Appl. Geochem.* **82**, 89-101.

882 Kalogeropoulos S. I. and Scott S. D. (1983) Mineralogy and geochemistry of tuffaceous
883 exhalites (tetsusekiei) of the Fukazawa Mine, Hokuroku district, Japan. In *The*
884 *Kuroko and Related Volcanogenic Massive Sulfide Deposits* (eds. H. Ohmoto and
885 B. J. Skinner). Economic Geology Publishing Co., New Haven, CT, pp. 412-432.

886 Kato Y., Yamaguchi K. E. and Ohmoto H. (2006) Rare earth elements in Precambrian
887 banded iron formations: secular changes of Ce and Eu anomalies and evolution of
888 atmospheric oxygen. In *Evolution of Early Earth's Atmosphere, Hydrosphere, and*
889 *Biosphere-Constraints from Ore Deposits* (eds. S. E. Kesler and H. Ohmoto).
890 Geological Society of America, pp. 269-289.

891 Kitazono S. and Ueno H. (2003) Mineralogical and genetical aspects of the Doyashiki
892 Kuroko deposits, Hokuroku Basin, Japan. *Resour. Geol.* **53**, 143-153.

893 Komuro K., Kubota H., Sato T. and Tanimura S. (2004) Trace fossils and sulfur isotopes
894 in mudstones around the Kuroko deposits in the Hokuroku Basin, northeast Japan:
895 An attempt to delineate the depositional environment. *Resour. Geol.* **54**, 425-436.

896 Large R. R., McPhie J., Gemmell J. B., Herrmann W. and Davidson G. J. (2001) The
897 spectrum of ore deposit typres, volcanic environments, alteration halos, and
898 related exploration vectors in submarine volcanic successions: some examples
899 from Australia. *Econ. Geol.* **96**, 913-938.

900 Li J.-X., Qin K.-Z., Li G.-M., Evans N. J., Huang F. and Zhao J.-X. (2018a) Iron isotope
901 fractionation during magmatic-hydrothermal evolution: A case study from the
902 Duolong porphyry Cu-Au deposit, Tibet. *Geochim. Cosmochim. Acta* **238**, 1-15.

903 Li X., Wang J., Chu F., Wang H., Li Z., Yu X., Bi D. and He Y. (2018b) Variability of Fe
904 isotope compositions of hydrothermal sulfides and oxidation products at mid-
905 ocean ridges. *J. Marine Syst.* **180**, 191-196.

906 McLennan S. M. (1989) Rare earth elements in sedimentary rocks: Influence of
907 provenance and sedimentary processes. In *Geochemistry and Mineralogy of Rare*
908 *Earth Elements* (eds. B. R. Lipin and G. A. McKay). Mineralogical Society of
909 America, Washington, D.C., pp. 169-200.

910 Menor-Salván C., Tornos F., Fernández-Remolar D. and Amils R. (2010) Association
911 between catastrophic paleovegetation changes during Devonian–Carboniferous
912 boundary and the formation of giant massive sulfide deposits. *Earth. Planet. Sci.*
913 *Lett.* **299**, 398-408.

914 Miller C., Halley S., Green G. and Jones M. (2001) Discovery of the West 45 volcanic-
915 hosted massive sulfide deposit using oxygen isotopes and REE geochemistry.
916 *Econ. Geol.* **96**, 1227-1237.

917 Mills R. A. and Elderfield H. (1995) Rare earth element geochemistry of hydrothermal

deposits from the active TAG Mound, 26°N Mid-Atlantic Ridge. *Geochim. Cosmochim. Acta* **59**, 3511-3524.

Moeller K., Schoenberg R., Grenne T., Thorseth I. H., Drost K. and Pedersen R. B. (2014) Comparison of iron isotope variations in modern and Ordovician siliceous Fe oxyhydroxide deposits. *Geochim. Cosmochim. Acta* **126**, 422-440.

Mosier D. L., Berger V. I. and Singer D. A. (2009) *Volcanogenic Massive Sulfide Deposits of the World—Database and Grade and Tonnage Models*, U.S. Geological Survey Open-File Report 2009-1034, Reston, VA, 46 pp.

Nozaki T., Kato Y. and Suzuki K. (2013) Late Jurassic ocean anoxic event: evidence from voluminous sulphide deposition and preservation in the Panthalassa. *Sci. Rep.* **3**, 1889.

Ohmoto H. and Skinner B. J. (1983) *The Kuroko and Related Volcanogenic Massive Sulfide Deposits*. *Economic Geology Monographs* **5**, Economic Geology Publishing Co., New Haven, CT, 604 pp.

Ohmoto H. and Takahashi T. (1983) Geological setting of the Kuroko deposits, Japan: Part III. Submarine calderas and Kuroko genesis. In *The Kuroko and Related Volcanogenic Massive Sulfide Deposits* (eds. H. Ohmoto and B. J. Skinner). Economic Geology Publishing Co., New Haven, CT, pp. 39-54.

Ohmoto H. (1996) Formation of volcanogenic massive sulfide deposits: The Kuroko perspective. *Ore Geol. Rev.* **10**, 135-177.

Ohta A., Ishii S., Sakakibara M., Mizuno A. and Kawabe I. (1999) Systematic correlation of the Ce anomaly with the Co/(Ni+Cu) ratio and Y fractionation from Ho in distinct types of Pacific deep-sea nodules. *Geochem. J.* **33**, 399-417.

Ohta A. and Kawabe I. (2001) REE(III) adsorption onto Mn dioxide (δ-MnO_2) and Fe oxyhydroxide: Ce(III) oxidation by δ-MnO_2. *Geochim. Cosmochim. Acta* **65**, 695-703.

Planavsky N., Rouxel O., Bekker A., Shapiro R., Fralick P. and Knudsen A. (2009) Iron-oxidizing microbial ecosystems thrived in late Paleoproterozoic redox-stratified oceans. *Earth. Planet. Sci. Lett.* **286**, 230-242.

Planavsky N., Bekker A., Rouxel O. J., Kamber B., Hofmann A., Knudsen A. and Lyons T. W. (2010) Rare Earth Element and yttrium compositions of Archean and Paleoproterozoic Fe formations revisited: New perspectives on the significance and mechanisms of deposition. *Geochim. Cosmochim. Acta* **74**, 6387-6405.

Rouxel O., Fouquet Y. and Ludden J. N. (2004) Subsurface processes at the Lucky Strike hydrothermal field, Mid-Atlantic Ridge: Evidence from sulfur, selenium, and iron isotopes. *Geochim. Cosmochim. Acta* **68**, 2295-2311.

Rouxel O., Bekker A. and Edwards K. J. (2005) Iron isotope constraints on the Archean and Paleoproterozoic ocean redox state. *Science* **307**, 1088-1091.

956 Rouxel O., Shanks W. C., Bach W. and Edwards K. J. (2008) Integrated Fe- and S-isotope
957 study of seafloor hydrothermal vents at East Pacific Rise 9–10°N. *Chem. Geol.*
958 **252**, 214-227.

959 Rouxel O., Toner B., Germain Y. and Glazer B. (2018) Geochemical and iron isotopic
960 insights into hydrothermal iron oxyhydroxide deposit formation at Loihi
961 Seamount. *Geochim. Cosmochim. Acta* **220**, 449-482.

962 Sato T. (1974) Distribution and geological setting of the Kuroko deposits. *Mining Geol.*
963 *Spec. Issue* **6**, 1-9.

964 Schardt C. and Large R. R. (2009) New insights into the genesis of volcanic-hosted
965 massive sulfide deposits on the seafloor from numerical modeling studies. *Ore*
966 *Geol. Rev.* **35**, 333-351.

967 Severmann S., Johnson C. M., Beard B. L., German C. R., Edmonds H. N., Chiba H. and
968 Green D. R. H. (2004) The effect of plume processes on the Fe isotope
969 composition of hydrothermally derived Fe in the deep ocean as inferred from the
970 Rainbow vent site, Mid-Atlantic Ridge, 36°14′N. *Earth. Planet. Sci. Lett.* **225**, 63-
971 76.

972 Shanks W. C. and Thurston R. (2012) *Volcanogenic Massive Sulfide Occurrence Model*.
973 *U.S. Geological Survey Scientific Investigations Report* **2010–5070—C**, U.S.
974 Geological Survey Scientific Investigations Report, Denver, CO, 345 pp.

975 Sharma M., Polizzotto M. and Anbar A. D. (2001) Iron isotopes in hot springs along the
976 Juan de Fuca Ridge. *Earth. Planet. Sci. Lett.* **194**, 39-51.

977 Skulan J. L., Beard B. L. and Johnson C. M. (2002) Kinetic and equilibrium Fe isotope
978 fractionation between aqueous Fe(III) and hematite. *Geochim. Cosmochim. Acta*
979 **66**, 2995-3015.

980 Slack J. F., Grenne T., Bekker A., Rouxel O. J. and Lindberg P. A. (2007) Suboxic deep
981 seawater in the late Paleoproterozoic: Evidence from hematitic chert and iron
982 formation related to seafloor-hydrothermal sulfide deposits, central Arizona, USA.
983 *Earth. Planet. Sci. Lett.* **255**, 243-256.

984 Slack J. F., Grenne T. and Bekker A. (2009) Seafloor-hydrothermal Si-Fe-Mn exhalites in
985 the Pecos greenstone belt, New Mexico, and the redox state of ca. 1720 Ma deep
986 seawater. *Geosphere* **5**, 302-314.

987 Slack J. F. (2012) Exhalites. In *Volcanogenic Massive Sulfide Occurrence Model* (eds. W.
988 C. Shanks and R. Thurston). U.S. Geological Survey Scientific Investigations
989 Report, Denver, CO, pp. 159-168.

990 Syverson D. D., Borrok D. M. and Seyfried Jr W. E. (2013) Experimental determination
991 of equilibrium Fe isotopic fractionation between pyrite and dissolved Fe under
992 hydrothermal conditions. *Geochim. Cosmochim. Acta* **122**, 170-183.

993 Syverson D. D., Luhmann A. J., Tan C., Borrok D. M., Ding K. and Seyfried Jr W. E.

(2017) Fe isotope fractionation between chalcopyrite and dissolved Fe during hydrothermal recrystallization: An experimental study at 350°C and 500 bars. *Geochim. Cosmochim. Acta* **200**, 87-109.

Tanimura S., Date J., Takahashi T. and Ohmoto H. (1983) Geological setting of the Kuroko deposits, Japan: Part II. Stratigraphy and structure of the Hokuroku district. In *The Kuroko and Related Volcanic Massive Sulfide Deposits* (eds. H. Ohmoto and B. J. Skinner). Economic Geology Publishing Co., New Haven, CT, pp. 24-38.

Tornos F., Peter J. M., Allen R. and Conde C. (2015) Controls on the siting and style of volcanogenic massive sulphide deposits. *Ore Geol. Rev.* **68**, 142-163.

Tsukamoto Y., Nonaka K., Ishida A. and Kakegawa T. (2020) Geochemical and mineralogical studies of ca. 12 Ma hydrothermal manganese-rich rocks in the Hokuroku district in Japan. *Ore Geol. Rev.* **121**, 103539.

Tsutsumi M. and Ohmoto H. (1983) A preliminary oxygen isotope study of tetsusekiei ores associated with Kuroko deposits in the Hokuroku district, Japan. In *The Koroko and Related Volcanogenic Massive Sulfide Deposits* (eds. H. Ohmoto and B. J. Skinner). Economic Geology Publishing Co, New Heaven, CT, pp. 433-438.

Urabe T. and Marumo K. (1991) A new model for Kuroko-type deposits of Japan. *Episodes* **14**, 246-251.

Wang D., Sun X., Zheng Y., Wu S., Xia S., Chang H. and Yu M. (2017) Two pulses of mineralization and genesis of the Zhaxikang Sb–Pb–Zn–Ag deposit in southern Tibet: Constraints from Fe–Zn isotopes. *Ore Geol. Rev.* **84**, 347-363.

Wawryk C. M. and Foden J. D. (2015) Fe-isotope fractionation in magmatic-hydrothermal mineral deposits: A case study from the Renison Sn–W deposit, Tasmania. *Geochim. Cosmochim. Acta* **150**, 285-298.

Weyer S. and Schwieters J. B. (2003) High precision Fe isotope measurements with high mass resolution MC-ICPMS. *Int. J. Mass spectrom.* **226**, 355-368.

Yamada R. and Yoshida T. (2004) Volcanic sequences related to Kuroko mineralization in the Hokuroku district, northeast Japan. *Resour. Geol.* **54**, 399-412.

Yamada R. and Yoshida T. (2011) Relationships between Kuroko volcanogenic massive sulfide (VMS) deposits, felsic volcanism, and island arc development in the northeast Honshu arc, Japan. *Miner. Deposita* **46**, 431-448.

Yamada R., Yoshida T. and Kimura J.-I. (2012) Chemical and isotopic characteristics of the Kuroko-forming volcanism. *Resour. Geol.* **62**, 369-383.

Yamaguchi K. E., Johnson C. M., Beard B. L. and Ohmoto H. (2005) Biogeochemical cycling of iron in the Archean-Paleoproterozoic Earth: Constraints from iron isotope variations in sedimentary rocks from the Kaapvaal and Pilbara Cratons. *Chemical Geology* **218**, 135-169.

1032 Yokoyama T., Makishima A. and Nakamura E. (1999) Evaluation of the coprecipitation
1033 of incompatible trace elements with fluoride during silicate rock dissolution by
1034 acid digestion. *Chem. Geol.* **157**, 175-187.

1035 Zhu B., Zhang H.-F., Zhao X.-M. and He Y.-S. (2016) Iron isotope fractionation during
1036 skarn-type alteration: Implications for metal source in the Han-Xing iron skarn
1037 deposit. *Ore Geol. Rev.* **74**, 139-150.

1038 Zhu Z.-Y., Jiang S.-Y., Mathur R., Cook N. J., Yang T., Wang M., Ma L. and Ciobanu C.
1039 L. (2018) Iron isotope behavior during fluid/rock interaction in K-feldspar
1040 alteration zone – A model for pyrite in gold deposits from the Jiaodong Peninsula,
1041 East China. *Geochim. Cosmochim. Acta* **222**, 94-116.
1042

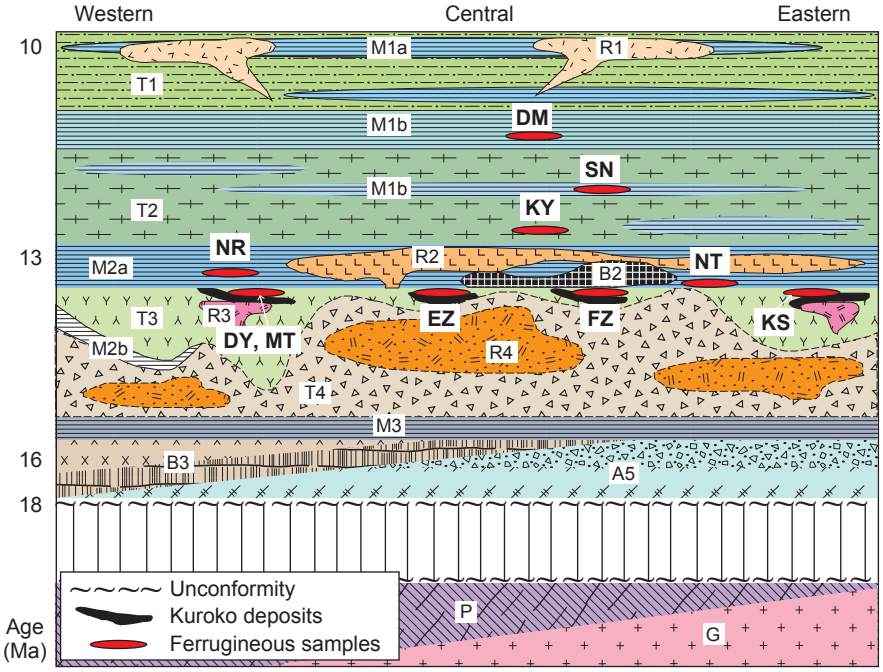

Fig. 1. Stratigraphy of the Hokuroku district (after Yamada et al., 2012). P = phyllite and chert basement; G = granitic rock; A5 = andesite lava flow, tuff breccia, and sandstone; B2 and B3 = pillow basalt, diabase sill, and basaltic tuff; M1–M3 = mudstone; T1–T4 = tuff (pumiceous tuff and tuff breccia) and volcanic breccia; R1–R4 = rhyolite. The ore horizon of Kuroko-type VMS mineralization occurs in the T3 tuff just below the M2a mudstone. Ferruginous sedimentary rock samples were taken from: DY = Doyashiki; MT = Matsumine; EZ = Ezuri; FZ = Fukazawa; KS = Kosaka; NT = Nittobe; NR = Nagatoro; KY = Koyukisawa; SN = Shinekari; DM = Daimyojin.

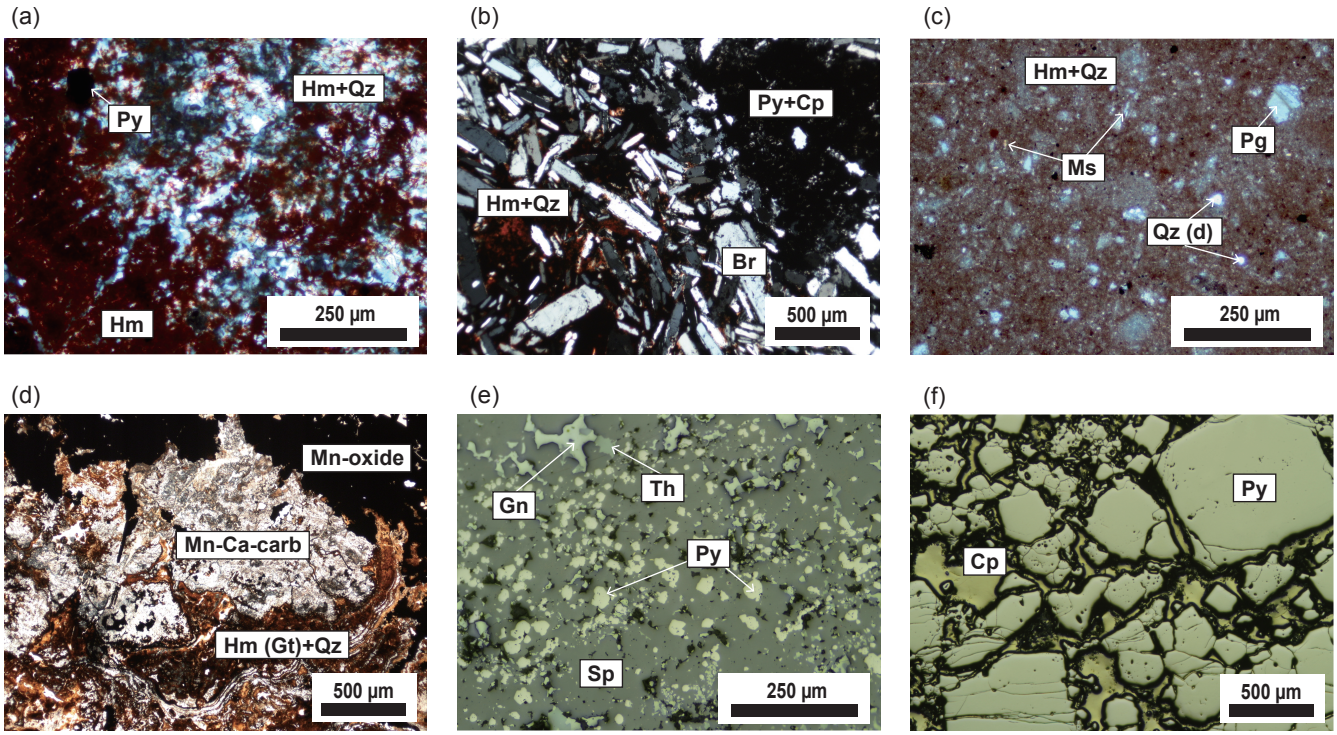

Fig. 2. Photomicrographs of ferruginous sedimentary rock and massive sulfide ore samples. (a) EZ4: ferruginous chert composed predominantly of microcrystalline quartz and hematite (XP; ×100); (b) KS3: barite-rich sample from the Kosaka deposit that is directly associated with massive sulfide ore (XP; ×50); (c) KS2: ferruginous chert containing some detrital materials from the Kosaka deposit (XP; ×100); (d) MT3: ferromanganese sample from the Matsumine deposit, consisting of alternating ferruginous and ferromanganese layers (XP; ×50); (e) FZ53: representative black ore (Zn–Pb-rich) from the Fukazawa deposit (RL; ×100); (f) MT54: representative yellow ore (Cu–Fe-rich) from the Matsumine deposit (RL; ×50). Hm = hematite; QZ = quartz; Br = barite; Py = pyrite; Cp = chalcopyrite; Mn–Ca-carb = Mn–Ca carbonates; Gt = goethite; Ms = muscovite; Pg = plagioclase; Qt(d) = detrital quartz; Gn = galena; Sp = sphalerite; Th = tetrahedrite; XP = cross-polarized transmitted light; RL = reflected light.

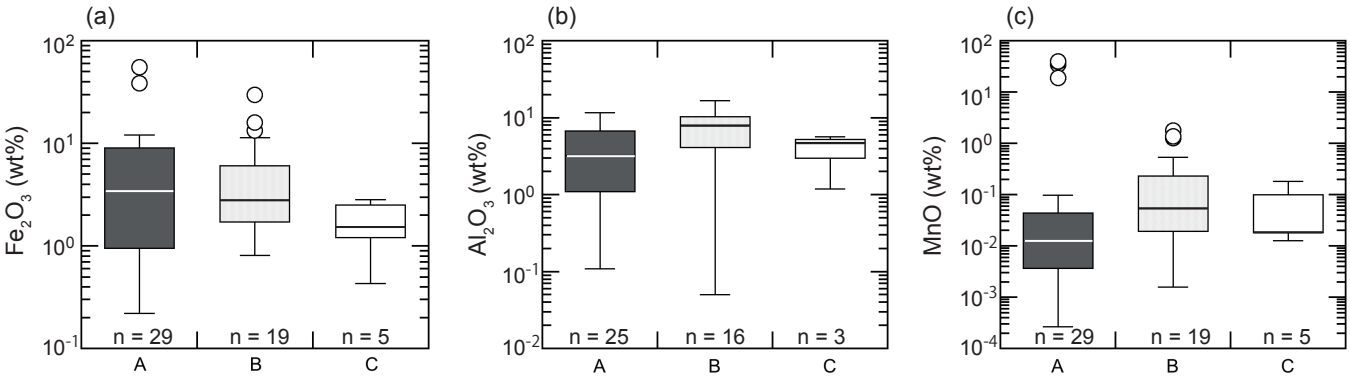

Fig. 3. Box plots of (a) Fe_2O_3, (b) Al_2O_3, and (c) MnO contents in Group A samples (associated with VMS deposits), and Group B and C samples (not associated with VMS deposits). Samples that were below XRF detection limits for Al_2O_3 (<0.05 wt.%) were excluded from (b).

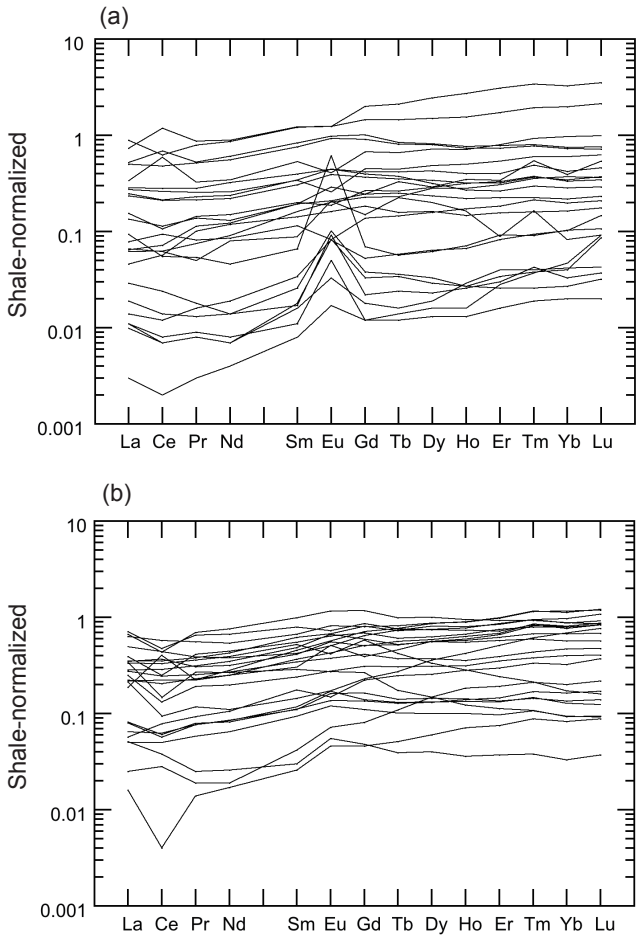

Fig. 4. Rare earth element (REE) patterns normalized to Post-Archean Australian Shale (PAAS; McLennan, 1989) for (a) Group A samples (associated with VMS deposits) and (b) Group B and C samples (not associated with VMS deposits).

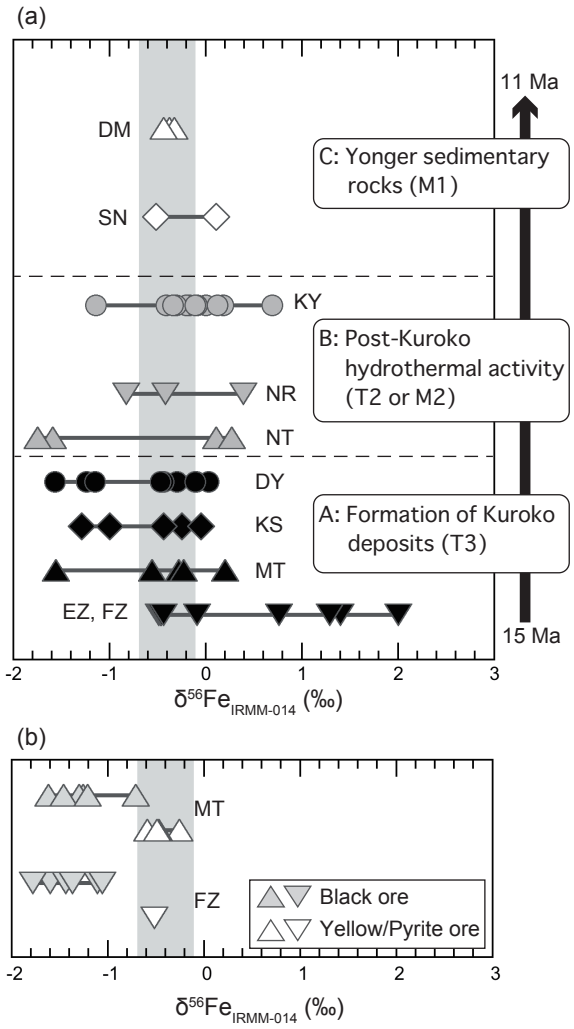

Fig. 5. $\delta^{56}Fe$ values of (a) ferruginous sedimentary rock samples plotted according to their stratigraphy and (b) sulfide ores from the Matsumine and Fukazawa deposits. Gray shaded areas indicate the $\delta^{56}Fe$ range for typical high-temperature, seafloor hydrothermal fluids (Sharma et al., 2001; Severmann et al., 2004; Rouxel et al., 2008). DY = Doyashiki; MT = Matsumine; EZ = Ezuri; FZ = Fukazawa; KS = Kosaka; NT = Nittobe; NR = Nagatoro; KY = Koyukisawa; SN = Shinekari; DM = Daimyojin.

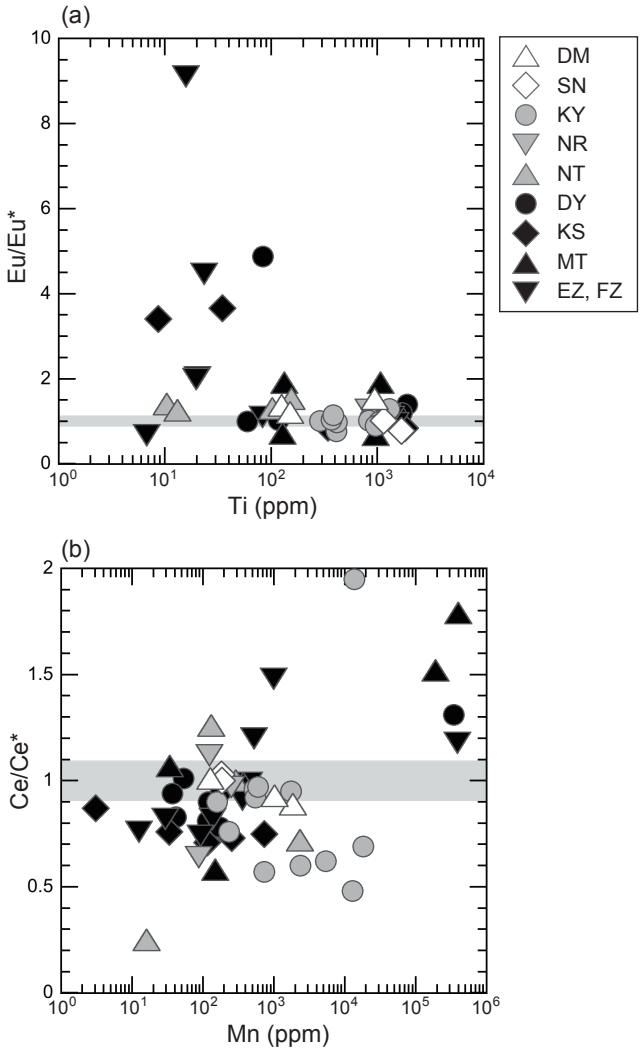

Fig. 6. Plots of the (a) Eu anomaly (Eu/Eu*) vs. Ti concentration and (b) Ce anomaly (Ce/Ce*) vs. Mn concentration for the ferruginous sedimentary rock samples.

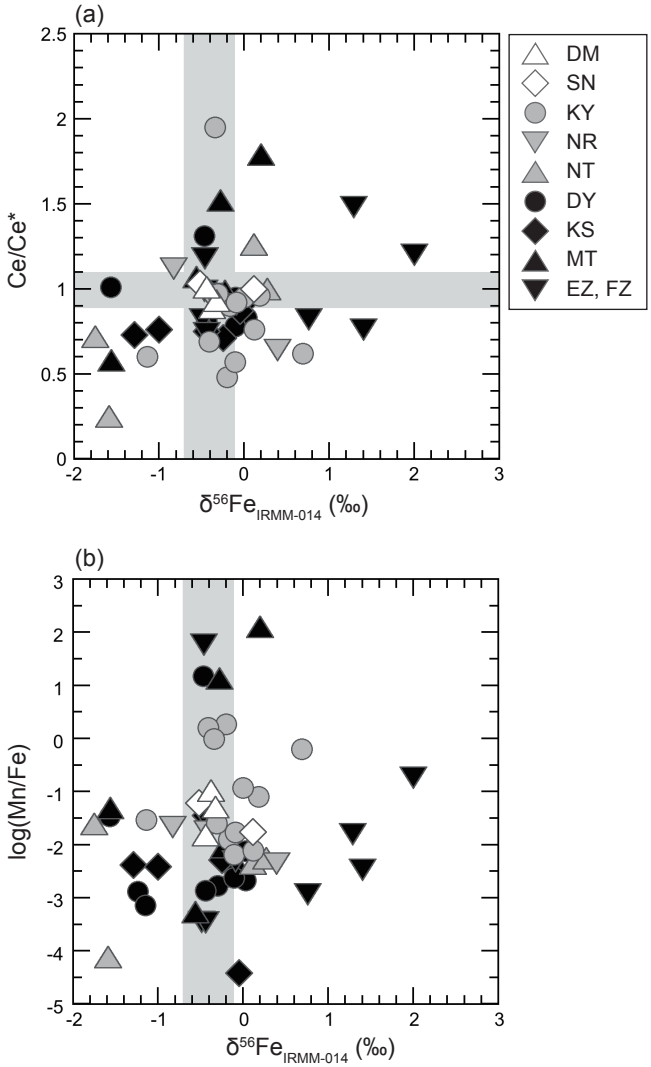

Fig. 7. Plots of the (a) Ce anomaly (Ce/Ce*) and (b) Mn/Fe ratios vs. $\delta^{56}Fe$ values for the ferruginous sedimentary rock samples. Gray shaded areas on the x-axis indicate the $\delta^{56}Fe$ range for typical high-temperature, seafloor hydrothermal fluids (Rouxel et al., 2008).

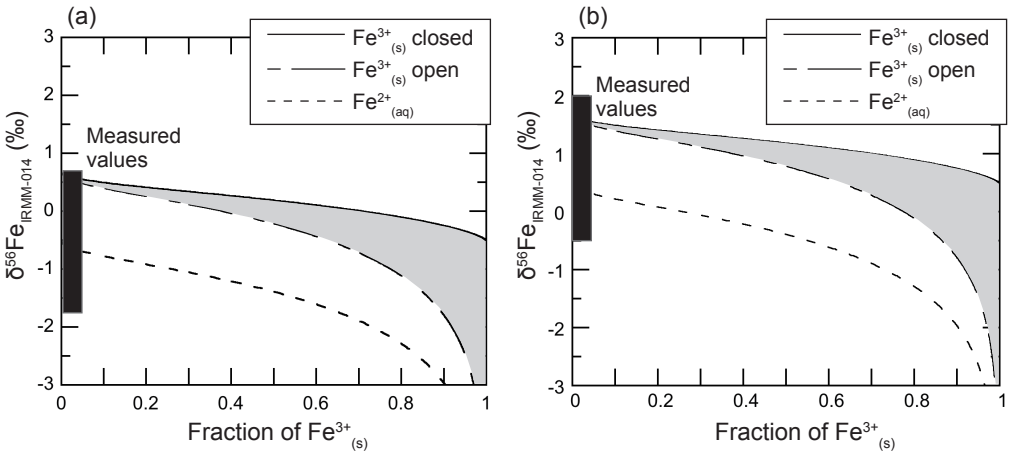

Fig. 8. Rayleigh-type model calculations for δ^{56}Fe values of precipitated ferric hydroxides from a $Fe^{2+}_{(aq)}$-bearing fluid as a function of the fraction of precipitated ferric iron ($Fe^{3+}_{(s)}$), assuming that the initial δ^{56}Fe value of Fe in the fluid is (a) –0.5‰ and (b) +0.5‰. The measured δ^{56}Fe range for most samples in Groups A and B are plotted in (a), whereas that for the Ezuri and Fukazawa deposits in Group A is plotted in (b). See the main text for description of the model and estimates of the parameters, including the fractionation factors.

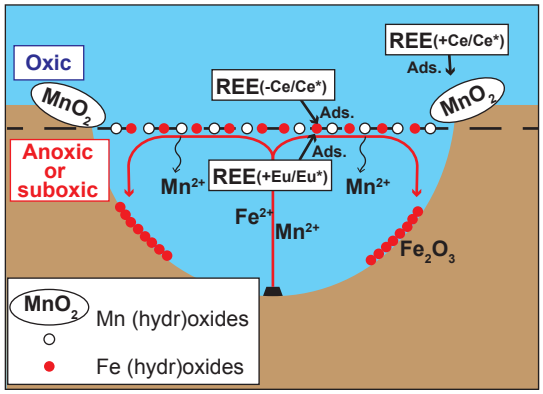

Fig. 9. Schematic diagram to illustrate geochemical behaviors of Fe and Mn as well as rare earth element (REE) signatures in a redox-stratified seawater. +Eu/Eu*, +Ce/Ce*, and -Ce/Ce* indicate positive Eu, positive Ce, and negative Ce anomalies, respectively. Ads. is an abbreviation for adsorption.

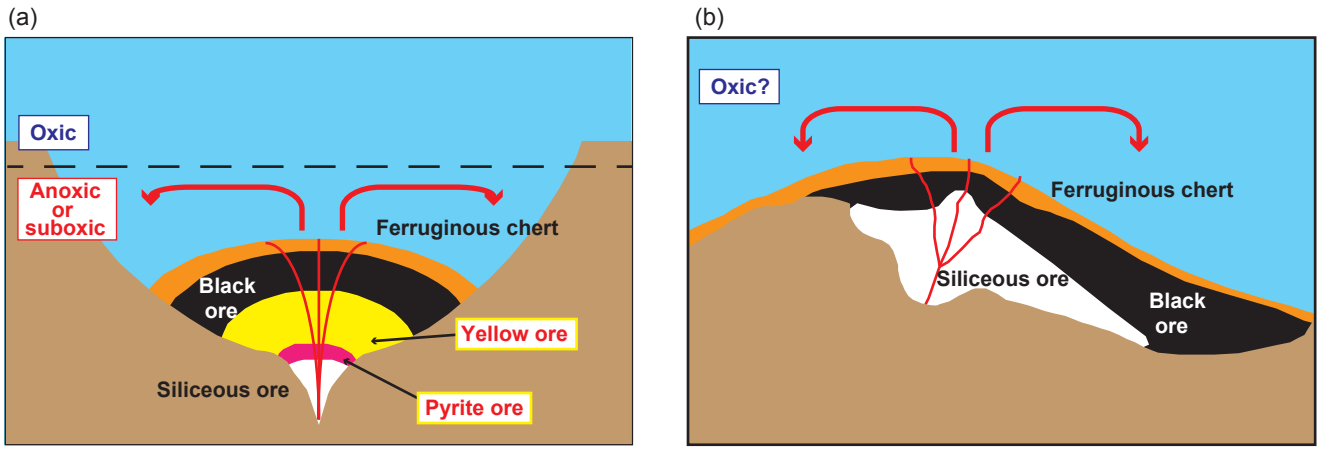

Fig. 10. Schematic diagram of the formation processes of sulfide ore bodies and ferruginous sedimentary rocks in the (a) Matsumine and (b) Fukazawa deposits.

Supplementary Data for

Large Fe isotope fractionations in sulfide ores and ferruginous sedimentary rocks from the Kuroko volcanogenic massive sulfide deposits in the Hokuroku district, northeast Japan

Tsubasa Otake, Ryoichi Yamada, Ryohei Suzuki, Shunsuke Nakamura, Akane Ito, Ki-cheol Shin, Tsutomu Sato

Corresponding author: Tsubasa Otake
Division of Sustainable Resources Engineering, Faculty of Engineering, Hokkaido University, N13W8, Kita-ku, Sapporo 060-8628, Japan
Phone: 011-706-6323; fax: 011-706-6323; e-mail: totake@eng.hokudai.ac.jp

Table of contents:

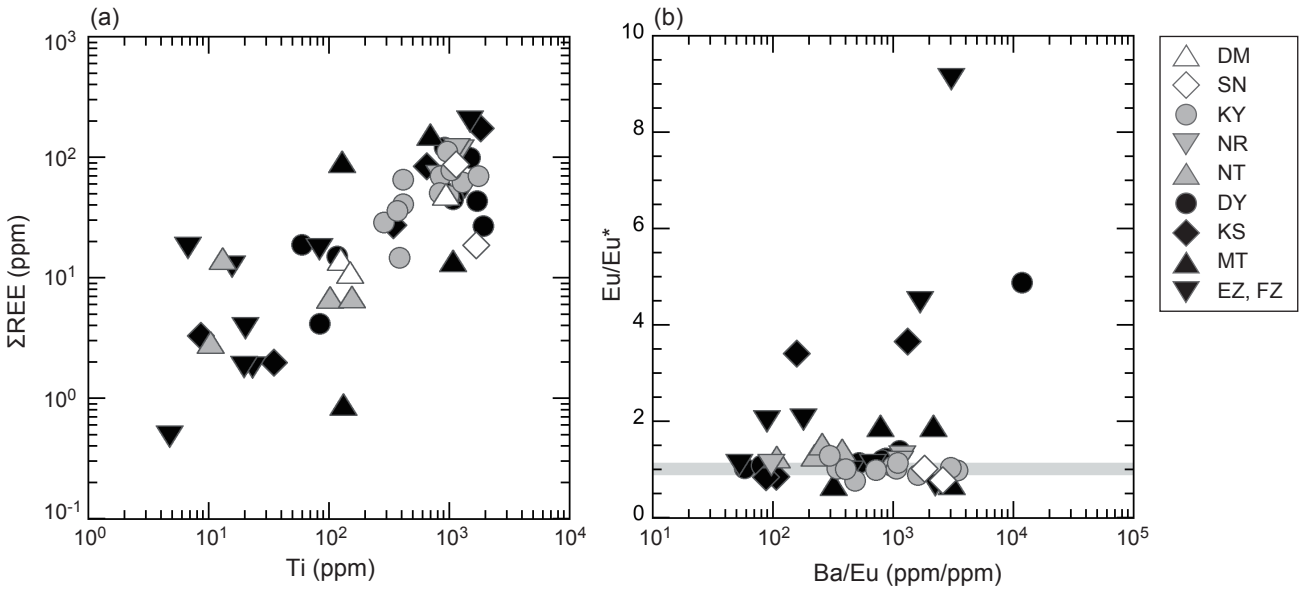

Fig. S1. Plots of the (a) ΣREE vs. Ti concentration and (b) Eu anomaly vs. Ba/Eu concentration ratio in ferruginous sedimentary rocks.

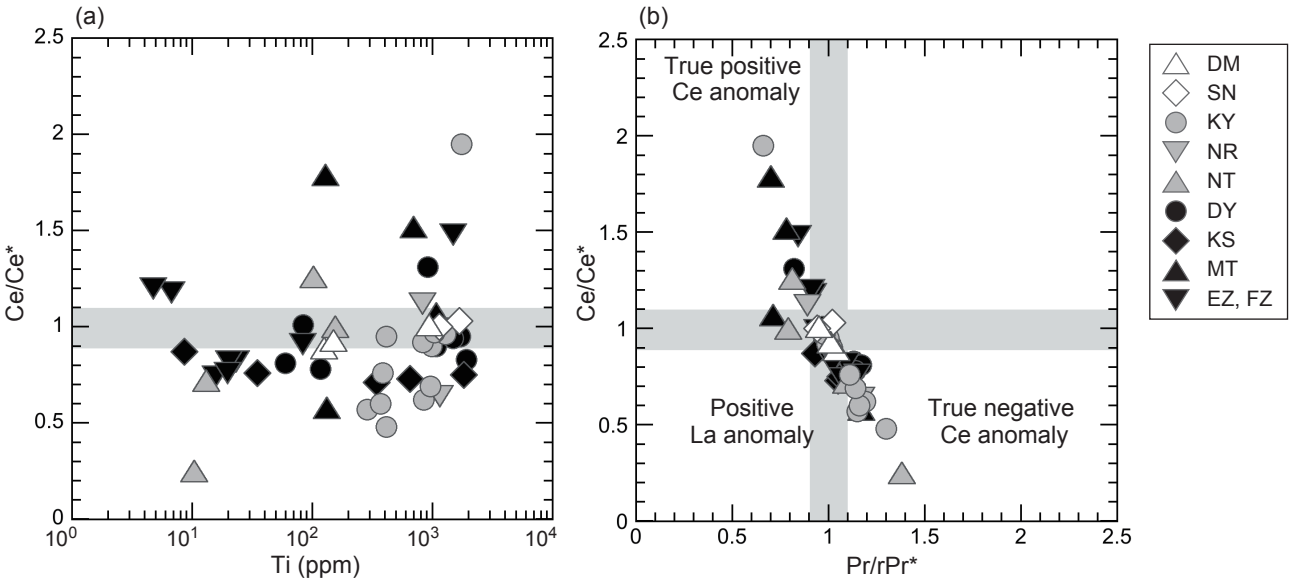

Fig. S2. Plots of the Ce anomaly vs. (a) Ti concentration and (b) Pr anomaly in ferruginous sedimentary rocks.

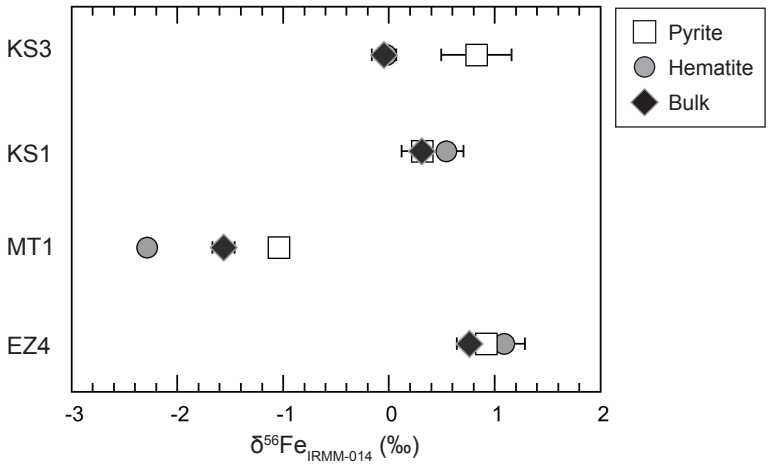

Fig. S3. Comparison of Fe isotope compositions of the bulk sample with those of physically separated pyrite and hematite in four Group A samples. The error bars indicate reproducibility of the analysis (2σ).

Supplementary Table 1. Major chemical compositions of ferruginous sedimentary rocks.

Sample ID	Group	SiO_2 (wt%)	Al_2O_3 (wt%)	Fe_2O_3 (wt%)	MnO (wt%)	MgO (wt%)	CaO (wt%)	Na_2O (wt%)	K_2O (wt%)	LOI (wt%)	TOTAL (wt%)	Comments
Doyashiki/Kannondo												
DY1	A	3.85	0.64	4.42	B.D.	0.18	B.D.	0.10	0.13	0.12	9.5	barite-rich
DY2	A	99.07	B.D.	0.54	B.D.	B.D.	B.D.	0.25	B.D.	0.00	100.1	
DY3	A	5.60	1.11	0.22	B.D.	0.15	B.D.	0.19	0.13	0.01	7.4	barite-rich
DY4	A	81.11	8.56	2.80	B.D.	0.42	0.11	0.25	2.22	3.92	99.4	
DY5	A	79.95	5.65	10.16	B.D.	0.56	0.12	0.33	2.54	2.82	102.2	
DY6	A	80.41	6.90	7.35	B.D.	0.53	0.11	0.27	2.19	3.46	101.3	
DY7	A	77.56	10.92	0.70	B.D.	B.D.	0.20	0.98	8.11	1.14	99.7	
DY8	A	79.63	1.58	12.14	B.D.	0.52	1.15	0.34	B.D.	7.18	102.6	
DY9	A	63.15	1.62	10.53	B.D.	0.57	6.06	0.16	B.D.	11.29	93.4	
DY10	A	28.57	4.27	3.32	44.39	0.83	13.08	0.50	B.D.	3.33	98.4	
Kosaka												
KS2	A	83.11	4.06	8.82	B.D.	1.01	0.34	0.26	1.36	0.09	99.2	
KS3	A	20.12	1.47	11.42	B.D.	0.21	0.13	B.D.	B.D.	10.80	44.3	barite-rich
KS4	A	19.62	B.D.	1.24	B.D.	B.D.	B.D.	0.54	B.D.	7.11	28.7	barite-rich
KS5	A	80.64	3.95	3.15	B.D.	3.54	0.46	0.88	1.02	5.99	99.7	
KS6	A	84.48	8.25	2.97	B.D.	2.78	0.43	0.64	1.09	0.15	100.9	
Eruzri												
EZ1	A	99.07	B.D.	0.54	B.D.	B.D.	B.D.	0.25	B.D.	1.25	101.3	
EZ2	A	30.59	3.37	55.50	B.D.	0.76	0.53	0.45	B.D.	2.32	93.9	
EZ3	A	89.78	6.04	1.69	B.D.	1.36	0.14	0.77	1.22	0.07	101.1	
EZ4	A	87.90	0.11	3.62	B.D.	0.10	0.08	0.23	0.02	8.30	100.4	
EZ5	A	30.44	B.D.	0.95	50.00	0.73	4.05	1.19	B.D.	12.06	99.6	
EZ6	A	58.90	1.06	38.63	B.D.	B.D.	0.53	2.57	0.10	0.72	103.0	
EZ7	A	96.61	0.73	0.41	B.D.	B.D.	B.D.	0.47	B.D.	1.17	99.7	
Matsumine												
MT1	A	15.03	1.01	0.43	B.D.	B.D.	B.D.	9.90	B.D.	9.05	35.6	barite-rich
MT2	A	82.08	6.80	9.05	B.D.	0.14	B.D.	B.D.	1.68	0.23	100.1	
MT3	A	59.13	3.13	2.00	24.72	0.74	5.41	0.48	0.52	0.37	96.7	
MT4	A	32.25	1.64	0.45	51.54	0.36	3.24	0.30	B.D.	8.81	98.7	
MT5	A	69.33	11.69	5.85	0.12	2.49	1.69	2.05	2.17	7.94	103.4	
Fukazawa												
FZ1	A	70.34	8.86	8.97	B.D.	2.90	0.13	0.13	1.84	6.07	99.3	
FZ2	A	83.60	1.10	10.57	B.D.	0.22	0.50	0.18	B.D.	4.62	100.9	
Nittobe												
NT1	B	68.42	B.D.	29.94	B.D.	0.11	0.06	0.54	B.D.	0.90	100.0	
NT2	B	96.22	0.26	4.20	B.D.	0.14	B.D.	B.D.	B.D.	0.02	101.0	
NT3	B	86.06	0.05	13.41	0.23	0.07	0.06	B.D.	B.D.	0.02	100.0	
NT4	B	80.47	2.56	7.41	B.D.	2.44	0.31	0.36	B.D.	2.84	96.5	
Nagatoro												
NR1	B	82.96	10.39	0.81	B.D.	0.10	0.70	2.43	3.32	0.06	100.8	
NR2	B	77.94	12.64	2.00	B.D.	0.90	1.02	2.93	3.86	0.10	101.4	
NR3	B	68.25	16.88	2.80	B.D.	5.84	0.83	0.55	0.31	1.88	97.4	
Koyukisawa												
KY1	B	77.80	7.93	1.80	B.D.	0.28	0.16	2.82	2.01	1.11	93.9	
KY2	B	79.12	6.45	0.95	B.D.	0.39	0.33	0.74	3.58	2.00	93.6	
KY3	B	83.56	8.93	2.10	0.22	1.30	0.55	1.76	2.29	3.64	104.4	
KY4	B	79.38	8.15	0.99	1.67	0.41	3.74	3.17	1.62	5.71	104.9	
KY5	B	80.74	10.40	1.23	0.66	0.43	0.56	4.23	2.12	3.86	104.4	
KY6	B	79.15	8.58	4.67	B.D.	3.45	0.59	0.76	2.80	4.84	104.9	
KY7	B	84.54	5.68	3.42	B.D.	1.37	0.40	0.47	2.10	3.09	101.2	
KY9	B	77.34	B.D.	16.04	B.D.	1.83	0.66	0.54	B.D.	3.49	100.0	
KY10	B	74.57	B.D.	11.41	0.28	1.02	0.34	0.87	2.44	8.86	99.8	
KY11	B	77.66	7.52	1.63	2.35	0.75	6.38	1.60	2.68	0.16	100.8	
KY12	B	74.19	13.93	1.98	1.77	1.14	2.60	2.93	1.67	0.37	100.6	
KY8	B	79.50	2.41	4.33	0.17	1.56	0.97	1.16	3.04	6.35	99.5	
Shinekari												
SN1	C	95.82	B.D.	0.43	B.D.	0.61	B.D.	0.58	1.45	0.64	99.6	
SN2	C	90.79	5.64	1.54	B.D.	1.30	B.D.	0.68	0.88	0.10	101.0	
Daimiyojin												
DM1	C	83.26	1.20	2.53	0.24	2.59	0.34	0.72	1.46	7.52	99.9	
DM2	C	92.37	B.D.	2.83	0.13	1.84	0.32	0.74	1.16	0.44	99.8	
DM3	C	91.69	4.78	1.21	B.D.	0.36	0.15	0.46	1.81	0.10	100.6	

LOI: Loss of ignition; B.D.: Below detection limit (<0.01–0.05 wt%)

Supplementary Table 2-1. Trace element compositions of ferruginous sedimentary rocks.

Sample ID	Group	Sc (ppm)	Ti (ppm)	Mn (ppm)	Co (ppm)	Ni (ppm)	Cu (ppm)	Zn (ppm)	Sr (ppm)	Y (ppm)	Zr (ppm)	Ba (ppm)	Pb (ppm)	Th (ppm)	U (ppm)	ΣREE (ppm)
Doyashiki/Kannondo																
DY1	A	B.D.	171	40.4	B.D.	1.95	46800	2870	7680	8.50	13.9	531000	2980	0.97	1.29	N.A.
DY2	A	B.D.	55.0	2.69	0.83	3.16	87300	1920	27.5	0.95	B.D.	20.4	31.2	B.D.	1.01	N.A.
DY3	A	1.09	83.7	53.1	0.47	12.3	85.0	1310	483	0.97	7.13	1210	276	0.18	4.23	4.17
DY4	A	8.80	1910	41.5	1.53	9.10	16.8	50.7	14.0	7.06	55.6	356	29.9	4.51	1.15	27.0
DY5	A	6.34	1070	119	3.29	18.2	13.4	93.3	14.5	5.12	37.6	417	20.5	2.49	0.70	44.8
DY6	A	7.89	1700	179	6.24	17.1	15.9	73.1	15.5	7.34	53.1	346	33.4	3.92	0.89	43.4
DY7	A	7.12	1490	37.0	0.90	1.41	2.63	156	18.2	17.5	156	519	9.74	5.95	6.24	99.9
DY8	A	B.D.	59.4	116	0.99	6.20	B.D.	B.D.	42.2	6.22	7.64	20.8	40.9	B.D.	5.16	18.8
DY9	A	0.66	117	175	0.24	9.08	32.7	26.9	67.8	3.93	6.82	10.1	5.65	0.23	2.73	15.1
DY10	A	5.36	907	N.A.	48.1	728	316	204.9	51.8	22.6	36.8	84.8	85.3	2.36	2.19	121
Kosaka																
KS2	A	4.68	650	255	0.10	5.65	8.44	33.2	35.6	22.2	51.0	10200	57.4	3.21	3.05	84.4
KS3	A	0.25	8.59	3.05	0.44	0.75	26800	128	148	0.54	2.93	17	156	B.D.	7.58	3.29
KS4	A	0.67	34.7	33.5	0.84	8.33	85300	967	117	1.38	3.09	118	181	0.04	9.88	1.98
KS5	A	1.30	342	114	1.08	12.4	4.49	14.0	9.34	8.97	2.24	21.7	6.02	0.67	0.12	27.4
KS6	A	9.71	1820	730	4.92	62.6	16.4	53.2	54.2	86.0	82.9	117	40.3	5.56	1.18	174
Eruzri																
EZ1	A	B.D.	19.6	12	0.69	4.97	B.D.	179	2.49	1.35	B.D.	15.9	9.60	B.D.	0.64	1.82
EZ2	A	0.29	23.2	135	0.36	20.7	248	27.0	87.2	0.32	1.11	89.5	479	0.13	6.19	1.81
EZ3	A	8.77	1340	446	1.61	14.3	1.32	194	30.5	9.75	65.9	324	5.67	4.08	1.26	56.8
EZ4	A	0.42	20.2	29.4	0.09	1.06	B.D.	B.D.	2.45	1.70	2.74	15.8	50.1	0.07	1.75	3.83
EZ5	A	0.29	6.70	N.A.	0.36	4.62	20.6	32.9	15.5	3.19	1.04	202	16.5	0.10	0.90	17.7
EZ6	A	B.D.	15.7	92.2	0.65	1.99	242	B.D.	59.6	2.61	B.D.	2020	467	B.D.	21.8	12.4
EZ7	A	0.16	4.74	522	0.04	0.92	3.90	16.6	1.37	0.72	0.68	7.54	3.96	0.02	0.16	0.48
Matsumine																
MT1	A	0.29	132	147	0.43	1.11	564	404000	49.9	0.15	8.73	39.9	7250	0.06	1.15	0.89
MT2	A	3.45	1070	34.1	8.68	33.8	5780	43.8	4.74	3.94	122	176	60.8	5.71	15.4	13.9
MT3	A	4.50	693	N.A.	5.55	54.3	45.0	135	273	32.1	41.2	11200	127	2.39	3.37	155
MT4	A	2.28	128	N.A.	7.03	66.0	142	351	104	15.0	5.86	1350	99.2	0.21	3.92	92.2
MT5	A	4.07	958	370	43.4	4.88	1180	239	7.25	14.5	116	90.0	216	5.13	3.71	53.6
Fukazawa																
FZ1	A	8.74	1480	993	2.39	B.D.	B.D.	B.D.	68.6	35.1	240	120	8.89	5.25	1.69	198
FZ2	A	1.09	82.9	358	1.74	14.8	695	72.2	23.2	6.09	3.35	11.5	61.8	0.15	0.83	17.3
Nittobe																
NT1	B	0.19	10.4	15.9	0.23	5.17	15.7	1.21	1.35	1.48	1.52	18.7	1.22	0.02	0.07	2.92
NT2	B	2.74	102	130	1.77	22.5	28.8	448	5.82	5.82	8.33	17.1	4.72	0.11	0.21	6.92
NT3	B	0.71	13.0	2310	8.93	23.1	84.8	930	4.63	2.77	7.65	18.7	4.98	0.08	0.11	14.5
NT4	B	4.46	155	289	4.74	12.7	21.3	30.6	13.2	1.07	3.91	15.1	2.08	0.06	0.19	6.98
Nagatoro																
NR1	B	6.09	824	122	B.D.	B.D.	7.06	18.8	82.4	16.8	143	721	34.8	7.25	2.13	70.2
NR2	B	6.90	1240	250	0.08	2.82	7.90	57.5	115	23.1	215	1010	13.9	11.2	2.82	114
NR3	B	6.12	1150	86.2	4.87	3.33	3.99	65.6	50.6	26.5	165	122	5.44	5.65	1.11	117
Koyukisawa																
KY1	B	5.02	985	157	0.40	1.25	2.38	38.3	20.4	16.1	107	157	3.57	4.38	1.17	48.0
KY2	B	7.94	1290	528	12.2	30.3	26.8	133	43.5	14.8	78.5	215	33.3	3.48	2.64	62.0
KY3	B	8.42	412	1740	4.69	17.5	23.7	93.1	19.4	9.03	7.43	219	39.3	1.71	0.47	65.2
KY4	B	2.32	415	N.A.	2.39	45.7	8.23	35.7	18.5	4.49	5.52	1020	20.2	0.96	0.53	40.8
KY5	B	4.38	847	5440	4.33	18.7	3.58	60.4	66.5	23.6	101	685	3.20	5.19	1.01	70.0
KY6	B	3.58	832	550	7.43	52.4	4.69	108	40.6	9.77	55.5	431	23.5	3.64	0.68	50.9
KY7	B	6.65	1040	601	3.41	37.4	23.7	71.5	45.1	26.1	33.0	526	20.0	3.05	0.68	78.4
KY9	B	14.0	287	736	14.7	34.9	25.9	2860	58.2	10.4	12.3	75.2	13.9	0.10	0.41	28.8
KY10	B	1.61	369	2360	11.4	12.5	15.2	21.3	87.8	8.30	61.5	897	20.4	2.58	0.68	36.1
KY11	B	4.92	960	N.A.	7.57	48.0	30.7	39.3	70.9	21.6	96.7	1260	20.8	5.40	1.63	112
KY12	B	6.52	1750	N.A.	19.1	117	14.4	99.3	650	24.7	281	5640	10.3	12.3	2.62	70.2
KY8	B	1.95	384	232	1.01	18.9	4.18	20.4	12.2	3.48	11.7	161	4.66	0.62	0.38	14.7
Shinekari																
SN1	C	4.15	1670	181	2.76	13.2	30.9	51.9	9.99	3.41	64.3	418	67.3	0.84	1.06	18.7
SN2	C	9.74	1140	185	B.D.	9.10	4.77	57.7	30.0	21.9	82.3	1004	8.77	4.80	3.88	87.1
Daimiyojin																
DM1	C	1.18	125	N.A.	0.34	1.31	1.96	16.8	7.97	3.19	10.1	70.2	2.91	0.63	0.27	14.2
DM2	C	0.99	150	N.A.	1.14	4.54	5.98	33.6	6.50	2.65	7.67	28.2	5.54	0.47	0.28	11.1
DM3	C	9.15	937	127	1.60	68.8	36.8	57.4	97.2	15.2	86.9	3470	23.7	4.49	4.28	49.1

B.D.: Below detection limit (< 0.01–0.05 ppm); N.A.: Not available

*Concentrations of some elements (e.g., Ba, Sr) may be underestimated because of incomplete digestion of barite-rich samples.

Supplementary Table 2-2. Trace element (REEs) compositions of ferruginous sedimentary rocks.

Sample ID	Group	La (ppm)	Ce (ppm)	Pr (ppm)	Nd (ppm)	Sm (ppm)	Eu (ppm)	Gd (ppm)	Tb (ppm)	Dy (ppm)	Ho (ppm)	Er (ppm)	Tm (ppm)	Yb (ppm)	Lu (ppm)
Doyashiki/Kannondo															
DY1	A	N.A.	N.A.	N.A.	N.A.	N.A.	N.A.	N.A.	N.A.	N.A.	N.A.	N.A.	N.A.	N.A.	N.A.
DY2	A	N.A.	N.A.	N.A.	N.A.	N.A.	N.A.	N.A.	N.A.	N.A.	N.A.	N.A.	N.A.	N.A.	N.A.
DY3	A	1.10	1.88	0.16	0.46	0.10	0.10	B.D.	0.02	0.11	0.03	0.08	0.02	0.09	0.02
DY4	A	5.21	9.05	1.22	4.43	1.08	0.32	1.14	0.26	1.37	0.35	0.97	0.22	1.11	0.24
DY5	A	9.43	17.10	2.04	8.10	1.91	0.48	1.85	0.29	1.49	0.27	0.76	0.12	0.80	0.13
DY6	A	8.93	16.88	1.90	7.47	1.70	0.42	1.71	0.27	1.60	0.32	0.91	0.15	0.98	0.16
DY7	A	19.04	38.09	4.59	18.84	4.25	1.00	4.24	0.63	3.76	0.73	2.10	0.31	2.05	0.31
DY8	A	2.48	5.74	1.01	4.15	1.08	0.23	1.15	0.20	1.09	0.22	0.64	0.09	0.61	0.10
DY9	A	1.77	4.56	0.89	4.02	0.79	0.17	0.86	0.12	0.76	0.15	0.45	0.06	0.46	0.08
DY10	A	19.95	55.02	4.67	20.53	4.65	1.06	4.74	0.66	3.84	0.77	2.22	0.33	2.12	0.33
Kosaka															
KS2	A	18.00	25.78	3.62	15.63	3.61	N.A.	4.10	0.66	4.31	0.91	2.76	0.45	3.04	0.50
KS3	A	0.72	1.09	0.11	0.46	0.14	0.11	0.17	0.03	0.16	0.03	0.10	0.02	0.11	0.04
KS4	A	0.41	0.56	0.07	0.24	0.10	0.09	0.15	0.03	0.13	0.03	0.07	0.01	0.08	0.01
KS5	A	5.97	8.48	1.27	5.10	1.11	0.20	1.24	0.21	1.35	0.31	0.94	0.15	0.95	0.15
KS6	A	34.05	49.84	6.96	29.19	6.73	1.34	9.37	1.64	11.50	2.72	8.89	1.38	9.24	1.52
Eruzri															
EZ1	A	0.36	0.53	0.07	0.24	0.09	0.04	0.08	0.01	0.09	0.03	0.11	0.02	0.12	0.02
EZ2	A	0.43	0.66	0.08	0.28	0.06	0.05	0.05	0.01	0.06	0.01	0.04	0.01	0.06	0.01
EZ3	A	10.88	22.32	2.50	10.97	2.20	0.48	1.95	0.33	2.01	0.40	1.14	0.20	1.20	0.20
EZ4	A	0.53	0.96	0.14	0.64	0.19	0.09	0.25	0.04	0.30	0.07	0.24	0.04	0.29	0.06
EZ5	A	2.98	7.50	0.73	2.87	0.64	0.09	0.64	0.11	0.74	0.17	0.53	0.09	0.56	0.09
EZ6	A	3.58	4.39	0.48	1.57	0.37	0.66	0.33	0.04	0.29	0.07	0.26	0.04	0.29	0.05
EZ7	A	0.06	0.15	0.01	0.06	0.02	B.D.	0.04	0.01	0.05	0.01	0.03	B.D.	0.02	B.D.
Matsumine															
MT1	A	0.12	0.14	0.03	0.12	0.04	0.02	0.06	0.01	0.08	0.02	0.08	0.02	0.13	0.04
MT2	A	2.53	4.94	0.44	2.70	0.49	0.22	0.70	0.18	0.94	0.16	0.25	0.07	0.23	0.04
MT3	A	21.71	72.42	5.58	23.74	5.93	N.A.	6.14	1.02	6.51	1.38	4.21	0.65	4.43	0.68
MT4	A	12.96	47.60	2.90	11.71	2.95	0.44	3.16	0.51	3.38	0.71	2.29	0.38	2.74	0.43
MT5	A	10.5	20.9	2.27	8.80	1.89	0.28	2.10	0.34	2.27	0.50	1.55	0.24	1.70	0.27
Fukazawa															
FZ1	A	28.1	95.1	7.74	30.2	6.78	1.34	6.81	1.12	7.00	1.54	4.91	0.79	5.60	0.93
FZ2	A	2.37	4.99	0.67	3.07	0.90	0.22	1.07	0.18	1.32	0.28	0.88	0.15	1.06	0.16
Nittobe															
NT1	B	0.60	0.30	0.13	0.57	0.15	0.05	0.21	0.04	0.28	0.07	0.21	0.04	0.24	0.04
NT2	B	0.97	2.22	0.17	0.63	0.23	0.08	0.38	0.08	0.69	0.18	0.55	0.09	0.56	0.09
NT3	B	3.07	4.53	0.68	2.88	0.62	0.17	0.76	0.11	0.68	0.14	0.38	0.06	0.38	0.06
NT4	B	1.95	3.01	0.22	0.87	0.17	0.06	0.22	0.03	0.19	0.04	0.11	0.02	0.09	0.02
Nagatoro															
NR1	B	13.4	29.4	2.70	10.7	2.30	0.61	2.35	0.44	2.75	0.63	1.95	0.35	2.28	0.38
NR2	B	24.2	45.8	4.92	18.4	3.71	0.89	3.72	0.64	4.11	0.88	2.79	0.47	3.29	0.51
NR3	B	25.5	34.7	6.19	25.7	5.51	1.26	5.50	0.77	4.69	0.94	2.67	0.38	2.48	0.37
Koyukisawa															
KY1	B	8.48	16.3	2.04	8.46	2.05	0.46	2.39	0.40	2.64	0.57	1.77	0.27	1.91	0.30
KY2	B	10.9	23.0	2.78	11.8	2.69	0.72	2.76	0.41	2.63	0.55	1.64	0.24	1.60	0.25
KY3	B	12.8	26.3	3.18	13.3	2.92	0.45	2.72	0.33	1.57	0.28	0.69	0.09	0.49	0.07
KY4	B	13.0	11.7	2.38	9.02	1.59	0.30	1.25	0.14	0.69	0.12	0.32	0.04	0.26	0.04
KY5	B	15.0	20.0	3.67	15.2	3.07	0.69	3.22	0.47	2.95	0.67	2.14	0.32	2.24	0.36
KY6	B	10.6	19.6	2.25	9.11	1.91	0.41	1.93	0.29	1.74	0.35	1.11	0.18	1.32	0.20
KY7	B	13.5	28.2	3.37	14.5	3.45	0.73	3.78	0.56	3.53	0.77	2.46	0.38	2.76	0.47
KY9	B	8.12	7.51	1.04	3.74	0.80	0.19	1.07	0.21	1.69	0.42	1.46	0.25	1.94	0.33
KY10	B	9.57	10.5	1.70	6.72	1.34	0.30	1.45	0.24	1.46	0.31	1.00	0.15	1.13	0.18
KY11	B	27.17	37.7	5.76	22.8	4.39	0.79	4.02	0.59	3.49	0.73	2.06	0.34	2.17	0.36
KY12	B	7.23	32.4	2.00	9.50	2.52	N.A.	3.32	0.59	4.07	0.89	2.83	0.47	3.17	0.53
KY8	B	3.12	4.85	0.70	2.77	0.62	0.15	0.63	0.10	0.61	0.14	0.41	0.07	0.46	0.07
Shinekari															
SN1	C	2.17	6.18	0.82	3.59	0.98	0.16	1.04	0.19	1.20	0.28	0.85	0.14	0.91	0.16
SN2	C	19.0	35.1	3.42	12.89	2.35	0.55	3.02	0.57	3.80	0.80	2.42	0.38	2.48	0.40
Daimiyojin															
DM1	C	2.47	5.03	0.68	2.85	0.65	0.19	0.65	0.10	0.62	0.13	0.38	0.06	0.36	0.05
DM2	C	1.91	4.01	0.52	2.21	0.52	0.13	0.51	0.08	0.47	0.10	0.28	0.04	0.27	0.04
DM3	C	8.36	17.8	1.98	8.46	1.69	0.55	1.82	0.36	2.63	0.59	1.88	0.33	2.28	0.38

B.D.: Below detection limit (< 0.01 ppm); N.A.: Not available

Supplementary Table 3. Major and Trace element compositions of sulfide ores.

Sample ID	Ore type	Fe (wt%)	Cu (wt%)	Zn (wt%)	Pb (wt%)	Na (ppm)	Mg (ppm)	Al (ppm)	K (ppm)	Mn (ppm)	As (ppm)	Mo (ppm)	Cd (ppm)
Fukazawa													
FZ15	Black ore	2.19	3.12	36.88	1.63	149	2000	5070	1780	693	22.4	16.2	282
FZ22	Black ore	7.04	3.93	35.54	8.35	311	14900	8160	898	316	1.00	17.4	154
FZ27	Black ore	13.08	7.70	25.88	11.90	317	300	2670	2140	222	0.72	6.93	62.7
FZ29	Black ore	3.69	1.20	39.28	0.89	167	6110	8219	791	233	12.8	1.99	182
FZ31	Yellow ore	42.04	5.03	0.38	0.02	194	1340	1270	889	51	0.79	20.3	1.51
FZ53	Black ore	12.97	2.27	35.82	2.17	307	3540	3630	1890	349	1.01	5.15	110
FZ58	Black ore	3.47	1.60	30.78	5.81	149	2510	1300	668	155	75	12.2	165
Matsumine													
MT13	Black ore	0.23	1.12	38.07	3.53	160	B.D	145	666	837	68	0.63	261
MT37	Yellow ore	48.21	1.93	0.30	0.04	154	17	313	890	30	2.39	10.3	1.18
MT43	Black ore	0.87	0.44	31.93	4.97	131	59	180	668	501	23.5	3.31	198
MT54	Yellow ore	43.61	3.12	B.D	0.03	154	651	4830	2000	B.D	11.2	33.7	0.11
MT57	Black ore	17.88	30.32	4.31	7.68	258	B.D	287	1340	21	117	8.17	14
MT81	Pyrite ore	44.42	0.10	0.01	0.01	B.D	61510	5340	959	34	3.87	8.32	0.17
MT84	Pyrite ore	45.74	0.02	0.03	B.D	136	351	4570	2180	B.D	16	12.5	0.24
MT115	Black ore	0.19	0.70	18.06	3.54	99.2	B.D	142	662	231	23	0.53	133
MT119	Black ore	1.81	0.74	29.78	3.44	111	B.D	171	667	489	1.12	3.46	156
MT162	Black ore	3.13	2.05	31.63	1.25	220	134	13400	4120	227	7.04	4.64	161

B.D.: Below detection limit (< 0.01 wt% or 1 ppm)

Supplementary Table 4. Fe isotope compositions of ferruginous sedimentary rocks and sulfide ores.

Sample ID	δ^{56}Fe (‰)	2σ (n=3)	Sample ID	δ^{56}Fe (‰)	2σ (n=3)	Sample ID	δ^{56}Fe (‰)	2σ (n=3)
Ferrugnious sedimentary rocks						Sulfide ores		
Doyashiki/Kannondo			Nittobe			Fukazawa		
DY1	-1.24	0.05	NT1	-1.59	0.03	FZ15	-1.60	0.04
DY2	-1.15	0.09	NT2	0.11	0.06	FZ22	-1.44	0.03
DY3	-1.57	0.02	NT3	-1.75	0.04	FZ27	-1.37	0.02
DY4	0.03	0.03	NT4	0.27	0.03	FZ29	-1.78	0.04
DY5	-0.30	0.07				FZ31	-0.52	0.03
DY6	-0.10	0.02	Nagatoro			FZ53	-1.11	0.02
DY7	0.03	0.09	NR1	-0.83	0.05	FZ58	-1.06	0.07
DY8	-0.44	0.10	NR2	-0.42	0.02			
DY9	-0.11	0.03	NR3	0.39	0.03	Matsumine		
DY10	-0.47	0.07				MT13	-1.26	0.02
			Koyukisawa			MT37	-0.59	0.10
Kosaka			KY1	-0.17	0.07	MT43	-1.62	0.02
KS2	-1.29	0.04	KY2	0.18	0.10	MT54	-0.26	0.03
KS3	-0.05	0.06	KY3	0.00	0.02	MT57	-0.71	0.10
KS4	-1.00	0.02	KY4	-0.20	0.04	MT81	-0.47	0.01
KS5	-0.25	0.02	KY5	0.69	0.06	MT84	-0.49	0.02
KS6	-0.44	0.04	KY6	-0.09	0.08	MT115	-1.30	0.04
			KY7	-0.31	0.07	MT119	-1.46	0.01
Eruzri			KY9	-0.11	0.04	MT162	-1.21	0.04
EZ1	1.40	0.07	KY10	-1.14	0.07			
EZ2	-0.49	0.01	KY11	-0.41	0.04			
EZ3	-0.47	0.04	KY12	-0.34	0.04			
EZ4	0.76	0.10	KY8	0.12	0.10			
EZ5	-0.46	0.03						
EZ6	-0.44	0.10	Shinekari					
EZ7	2.00	0.06	SN1	-0.52	0.08			
			SN2	0.11	0.06			
Matsumine								
MT1	-1.56	0.05	Daimiyojin					
MT2	-0.56	0.06	DM1	-0.38	0.03			
MT3	-0.28	0.04	DM2	-0.33	0.07			
MT4	0.20	0.02	DM3	-0.44	0.05			
MT5	-0.23	0.05						
Fukazawa								
FZ1	1.29	0.05						
FZ2	-0.09	0.03						

*External reproducibility of a laboratory reference material was ±0.11‰ (2σ, n = 36).